Geomechanics and Engineering, *Vol. 43, No. 3 (2025) 167-195*
https://doi.org/10.12989/gae.2025.43.3.167

Period identification of multi degree of freedom structure-shallow foundation-ground system: Dynamic centrifuge test

Seong Jin Park[a], Dong Van Nguyen[b], Dookie Kim[c] and Yun Wook Choo*

Department of Civil and Environmental Engineering, Kongju National University (31080)
1223-24, Cheonan-daero, Seobuk-gu, Cheonan-si, Chungcheongnam-do (275 Budae-dong), Republic of Korea

(*Received July 1, 2025, Revised October 15, 2025, Accepted October 17, 2025*)

Abstract. This study aims to accurately identify periods of ground and lengthened period of multi-degree-of-freedom structures installed on shallow foundations in dynamic centrifuge model tests using the frequency domain decomposition (FDD) method. A series of dynamic centrifuge model tests were conducted with single- and multi-degree-of-freedom structures installed on shallow foundations and sandy ground. The frequency domain decomposition method was utilized to identify the ground period and the lengthened structure period. The results obtained from the FDD method for the soil–structure system, including periods and mode shapes, are compared with those calculated using conventional methods such as response spectrum (RS), ratio of response spectrum (RRS), fast Fourier transforms (FFT), and ratio of fast Fourier transforms (RFFT). The comparison demonstrates that FDD is effective in terms of both simplicity and accuracy for the modal analysis of complex soil–structure systems based on centrifuge test data.

Keywords: centrifuge modelling; frequency domain decomposition; lengthened structure period; multi-degree-freedom structure; natural period of ground; shallow foundations; soil-structure interaction

1. Introduction

Structures and grounds have their unique natural frequencies (or its inverse = natural periods) where their responses are amplified with earthquakes. The importance of the resonance phenomenon has been seriously recognized by a phenomenon of 'double resonance' observed in the severe damage at Mexico City earthquake in 1985 (Vucetic and Dobry 1987). This led to the increasing attention on determining both the natural periods of the ground and structure during seismic loadings, including seismic design of geotechnical structures (Kim *et al*. 2012, Lee *et al*. 2013, Kumar *et al*. 2024, Mostafaei and Soleimani Kutanaei 2025). Structures with flexible bottom boundary conditions have more degrees of freedom than structures with rigid conditions (Veletsos and Meek 1974), which means that the natural period of a structure determined by common numerical methods will differ from the actual period of a structure on the ground. This variability of the structure period is due to period lengthening, which is the main effect of soil-foundation-structure interaction (SFSI), and the rate of which depends on the ground properties and earthquake magnitude (ASCE 2021, Deviprasad and Dodagoudar 2020, Chaudhary *et al*. 2023, Kiani and Emami 2024, Lv *et al*. 2025). Furthermore, considering these SFSI, soil nonlinearity is essential. NIST (National Institute of Standards and Technology) has presented an equation that relates the ratio of flexible-base period (lengthened period) to fixed-base period to soil stiffness, taking nonlinearity into account (NIST 2012). Thus, it is critical to accurately determine the natural periods of the ground and lengthened period of structure for seismic design and understanding soil-structure interaction.

To investigate the dynamic response of a structure and its supporting ground subjected to an earthquake, centrifuge modeling has been popularly adopted with an inflight shaking table in a centrifuge equipment (Kim *et al*. 2012, Alshawmar and Fall 2021, Nagula *et al*. 2021). Either response spectra (RS) or fast Fourier transforms (FFT) are one of the most popular methods to analyze acceleration records of dynamic centrifuge model tests, especially determining the periods of the structure and ground (Freeman 2007, Lee *et al*. 2013, Kim *et al*. 2014, Yun and Han 2021, Soralump *et al*. 2025). However, all components in this kind of experiment interact and result in the complex acceleration records involved with the predominant period of the input earthquake motions, the natural period of the ground, and the natural period of the structure. In addition, undesirable reflected waves from container wall boundaries with modeled ground and noise generated during centrifugal acceleration are also possibly included into the instrument measurement (Teymur and Madabhushi 2003, Stringer *et al*. 2010). In the case where the peak acceleration of the input motions becomes strong and the number of degrees of freedom of the structure increases, it is more challenging to accurately separate the periods of the ground and structure due to the interaction between the components.

---

*Corresponding author, Professor
E-mail: ywchoo@kongju.ac.kr
[a]Ph.D. Student
[b]Research Professor
[c]Professor

ISSN: 2005-307X (Print), 2092-6219 (Online)

For the ground period, it is determined by the response spectrum ratio, which is the RS of the ground surface divided by the RS of the bedrock, minimizing the effects of the predominant period and noise contained in input seismic motion but highlighting the natural period of the ground in the recorded accelerations (Lee *et al*. 2013, Gillis 2015, Ko *et al*. 2019, Nguyen *et al*. 2023, Falcon 2024, Yun *et al*. 2024). The ratio of response spectra (RRS) has been quite a powerful tool to analyze the dynamic response of a single component system (i.e., either a ground only or a structure). However, the RRS often has limitations for a multiple-component system (i.e., a structure supported on the ground) to determine each period of the structure and ground due to their interactions. Higher degree-of-freedom structures produce multiple peaks for multiples modes in frequency spectra, leading to the complex response of the system.

The previously mentioned methods have struggled to difficultly extract periods from complex dynamic systems, particularly in the presence of overlapping dynamic responses such as soil response, structural response, and boundary reflection waves. To overcome these challenges, we apply the frequency domain decomposition (FDD) method, which is widely used for system identification of structures in the structural engineering field. The FDD method is capable of estimating mode shapes by performing singular value decomposition (SVD) on the power spectral density (PSD) of the acceleration response. Previous studies have applied FDD to structures to estimate their dynamic characteristics, but its application to ground-measured acceleration responses and soil-foundation-structure interaction problems remain limited (Jawalageri *et al*. 2022, Hadianfard and Kamli 2020, Qu *et al*. 2023, Hu *et al*. 2020, liyama *et al*. 2024, Hızal 2023, Hızal and Gül 2025).

Therefore, this study aims to accurately separate the ground period from multiple peaks from frequency response of complex acceleration signals (i.e., including the structural periods) measured at dynamic centrifuge tests. A series of dynamic centrifuge tests was performed with multi-degree of structures with shallow foundation installed on sandy ground. The FDD method was utilized to analyze acceleration records measured in the ground to extract mode shapes of the ground and the ground period from the frequency response of the complex system including structure, foundation, and soil. This enables a clearer identification of ground-specific dynamic behavior of structures: i.e., lengthened period of multi-degree-of-freedom (MDOF) structures subjected to earthquake.

2. Methodology

2.1 Frequency domain decomposition

Frequency domain decomposition (FDD) is one of the most popular techniques for identifying the modal parameters of a structure for system identification using only the output response, which retains the simplicity of the classical methods while overcoming their drawbacks. The FDD can effectively extract modal parameters, especially in lightly damped structures (Brincker *et al*. 2000). The theory of the FDD method is as follows.

Let x(t) be the unknown input signal and y(t) the measured response of the system. According to Bendat and Piersol (1986), the relationship between the power spectral densities (PSD) of input and output is given by

$$G_{yy}(j\omega) = \bar{H}(j\omega)G_{xx}(j\omega)H^T(j\omega) \tag{1}$$

Here, $G_{xx}(j\omega)$ is the PSD matrix of the input, $G_{yy}(j\omega)$ is the PSD matrix of the response, $H(j\omega)$ is the Frequency Response Function (FRF) matrix, and "$-$" and T is complex conjugate and transpose, respectively.

The FDD algorithm estimates the output PSD matrix $\hat{G}_{yy}(j\omega)$ from the measured response y(t), where a singular value decomposition (SVD) is applied at each frequency (ω_i). The natural period of the system can be estimated as the reciprocal of the frequency at which the singular value reaches its maximum. For more information, you can refer to the paper by Brincker *et al*. (2000).

Table 1 Specifications of KAIST centrifuge

Item	Specification
Model	C72-2
Platform radius	5.0 m
Maximum capacity	240 g-tons
Maximum acceleration	130 g with 1,300 kg payload
Maximum model payload	2,400 kg up to 100 g
Platform dimensions	1.2 m x 1.2 m x 1.2 m (L x W x H)

Table 2 Specifications of inflight shaking table

Item	Specification
Shaking type	Electro-hydraulic servo type
Shaking direction	One horizontal
Maximum model payload	700 kg
Payload dimensions	1.0 m x 0.8 m x 0.655 m (L x W x H)
Frequency range	20 ~ 300 Hz
Maximum acceleration	20 g (in model scale)

2.2 Centrifuge model tests

All the centrifuge tests were conducted at the Korea Advanced Institute of Science and Technology (KAIST) Geotechnical Centrifuge Testing Center (Kim *et al*. 2012). The specifications of the KAIST centrifuge are shown in Table 1. An equivalent shear beam (ESB) type container was used to minimize reflected wave at the container boundary by accommodating horizontal movement of the soil (Zeng and Schofield 1996). Its internal dimensions are 0.840 m x 0.630 m x 0.635 m (length x width x height).

2.2.1 Soil model

The soil specimens were prepared in ESB container by air-pluviating system, and Table 3 summarizes the soil properties. By adjusting the pouring mass rate, drop height, and sweep rate of the falling sand machine, the achieved

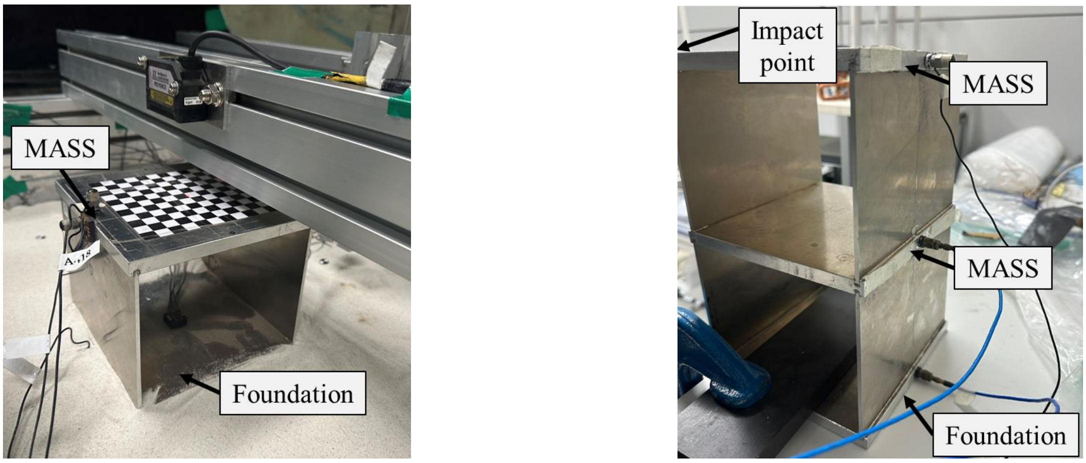

(a) (b)

Fig. 1 Pictures on (a) SDOF installed on soil model in centrifuge, and (b) impact Hammer test for 2DOF

Table 3 Soil Properties

Properties	Silica sand
Specific gravity, G_s	2.65
Maximum dry density, $\rho_{max}(t/m^3)$	1.607
Minimum dry density, $\rho_{min}(t/m^3)$	1.336
Grain size (mm)	$d_{10} = 0.067$
	$d_{50} = 0.164$
	$d_{60} = 0.189$
Soil classification, USCS	SP
Coefficient of uniformity, C_u	2.764
Angle of friction, $\phi(°)$	40.5

relative density of the soil was 77.10%. The dimensions of the soil are 0.840 m x 0.630 m x 0.600 m (length x width x height) in model scale, and 50.4 m x 37.8 m x 36 m (length x width x height) in prototype scale at 60 g.

2.2.2 Test model

The four test models were prepared. They include a horizontal free-field ground model and ground models with single-, two-, and three-degree-of-freedom structures installed on shallow foundations. The heights of the single-, two- and three-degree-of-freedom structures are 7.74 m, 14.88 m, and 22.02 m, respectively, at 60 g in prototype scale, and are made to target the approximate natural periods (T_a) of the 5-, 7-, and 11-story concrete structures (ASCE 2021).

$$T_a = 0.1N \tag{2}$$

Where N is the number of stories.

The test models are made of aluminum alloy, and the first fundamental period in prototype scale calculated from the mode analysis at fixed condition are 0.48 s, 0.82 s, and 1.16 s, respectively. An impact hammer test was also performed to experimentally measure dynamic characteristics of the structures (Fig. 1). The impact hammer test is well known as a modal test, which measures the response of a structure by applying a hammer force to a specimen to find its natural frequencies. As shown in Fig. 1, the foundation of the structure was simulated as a fixed end, and accelerometers were attached to each floor 'Mass' to perform the test. Table 4 summarizes the model structure properties.

The instruments used in the test were accelerometers (20-30 pieces; N600 to N100 denoted by 'North'; M550 to M50 denoted by 'Middle'; S600 to S100 denoted by 'South' in Fig. 2; Mass1 to Mass3, Foundation in Fig. 2) and bender elements (16 pairs; BE1 to BE16 in Fig. 2). The accelerometers were buried in the ground in three vertical arrays at three horizontal locations (North, Middle, and South in Fig. 2), where the accelerometers were vertically distributed at a constant distance of 10 cm at each array in the Fig. 2. The tips of each pair of bender elements were spaced 20 cm apart. The installed accelerometers measured the dynamic response of the ground during the earthquake. The bender element measured the shear wave velocity at the beginning, middle, and end of the series of earthquake excitations. A 5 kHz sine wave was transmitted and received using a sender bender element, and the measurement was made based on the point where the sine wave voltage first intersects the direct current (DC) level voltage (Youn *et al.* 2008). The initial average shear wave velocity of soil specimens measured using the bender element array was $V_s = 172.77\ m/s$ (average value of the entire soil layer) and $V_{s,30} = 164.61\ m/s$ (Eq. (3)). Thus, soil specimens were classified as DE ground by ASCE 7-22.

$$V_{s,30} = \frac{\sum_{i=1}^{n} d_i}{\sum_{i=1}^{n} \frac{d_i}{v_{si}}} \tag{3}$$

Here, n is soil layer number, d_i and v_{si} are the thickness and shear wave velocity of the layer, respectively, ranging from 0 to 30 m.

Additional accelerometers were attached to the bottom of the container and the structure to determine the characteristics of the input motion and the dynamic response of the structure (See Fig. 2).

2.2.3 Input motion and testing procedure

A total of five input motion were used: 1994

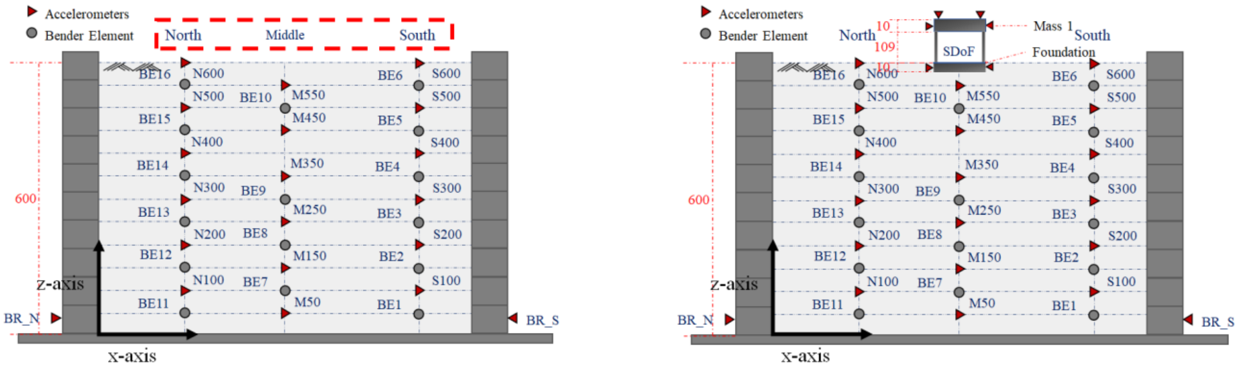

(a) Free Field condition (b) SDOF structure

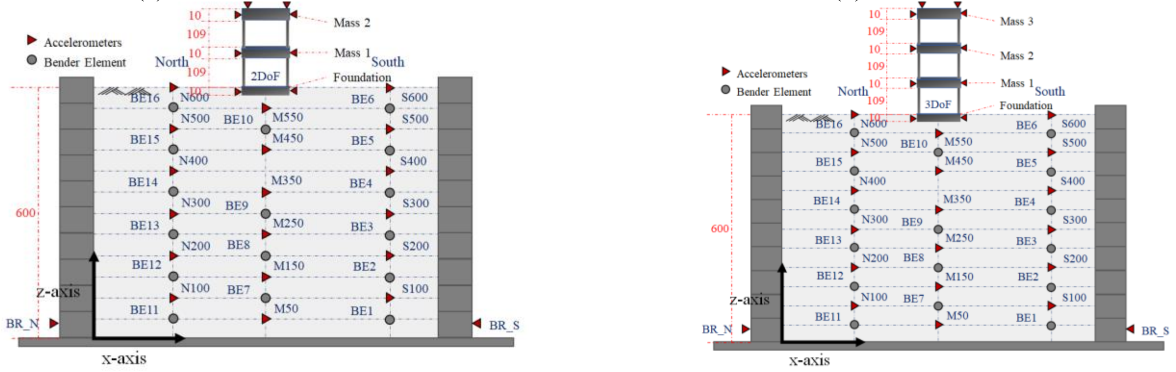

(c) 2DOF structure (d) 3DOF structure

Fig. 2 Experiment model setups (unit: mm)

Table 1 Model Structure Properties

	SDOF		2DOF		3DOF	
	Model	Prototype	Model	Prototype	Model	Prototype
						
Lumped mass $(L \times W \times d)$	0.15 x 0.15 x 0.01	9 x 9 x 0.6	0.15 x 0.15 x 0.01	9 x 9 x 0.6	0.15 x 0.15 x 0.01	9 x 9 x 0.6
Leg $(H \times W \times t)$	0.109 x 0.15 x 0.003	6.54 x 9 x 0.18	0.109 x 0.15 x 0.003	6.54 x 9 x 0.18	0.109 x 0.15 x 0.003	6.54 x 9 x 0.18
Foundation $(L \times W \times d)$	0.15 x 0.15 x 0.01	9 x 9 x 0.6	0.15 x 0.15 x 0.01	9 x 9 x 0.6	0.15 x 0.15 x 0.01	9 x 9 x 0.6
Mass (kg)	1.480	319,652	2.352	508,084	3.227	697,032
Effective mass m_S (kg)	0.7759	167,594	1.5543	335,729	2.2871	494,014
Column stiffness, k (N/m)	430948	25,856,872	430948	25,856,872	430948	25,856,872
Natural period, T_s (s)	0.008	0.48	T_1= 0.013 T_2= 0.005	T_1= 0.82 T_2= 0.3	T_1= 0.019 T_2= 0.006 T_3= 0.004	T_1= 1.16 T_2= 0.41 T_3= 0.27
Natural frequency, Numerical Analysis f_n (Hz)	123.22	2.08	f_1= 73.44 f_2= 197.27	f_1= 1.22 f_2= 3.28	f_1= 51.57 f_2= 147.93 f_3= 219.89	f_1= 0.86 f_2= 2.47 f_3= 3.66
Natural frequency, Impact hammer test f_n (Hz)	None*		f_1= 61.00 f_2= 167.54	f_1= 1.02 f_2= 2.80	f_1= 45.00 f_2= 132.00 f_3= 199.00	f_1= 0.75 f_2= 2.20 f_3= 3.30

*Failed to perform due to structure damage

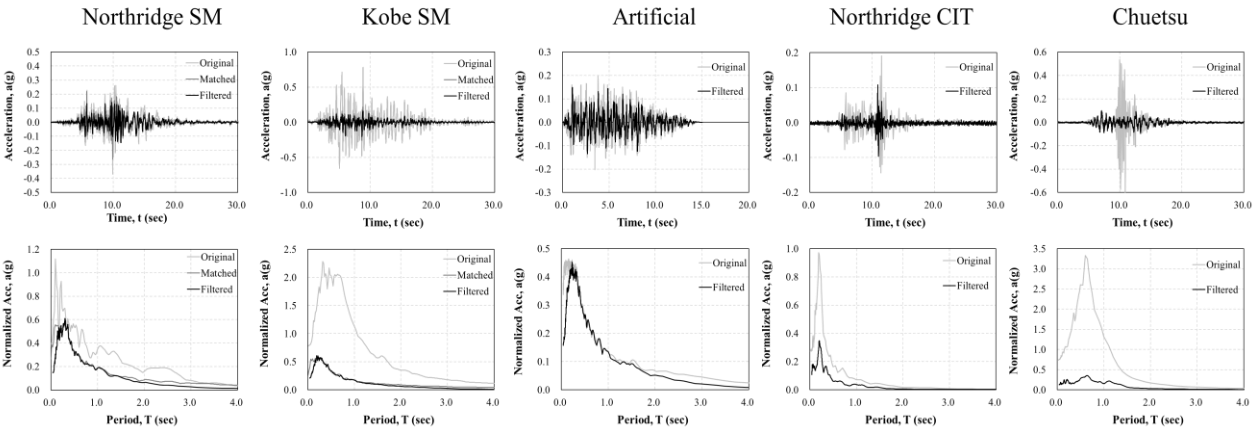

Fig. 3 Input motion and Response spectrum

Table 5 Free Field test (A1-1) PGA at bedrock

Free Field													
Sweep		Resweep		Kobe SM		Artificial		Northridge MW-CIT		Chuetsu		Northridge SM	
Event Number	PGA	Event Number	PGA	Event Number	PGA	Event Number	PGA	Event Number	PGA	Event Number	PGA	Event Number	PGA
001	0.008	004	0.001	014	0.012	022	0.012	030	0.010	037	0.017	04	0.011
002	0.011	005	0.011	015	0.013	023	0.014	031	0.011	038	0.022	050	0.021
003	0.012	006	0.014	016	0.040	024	0.032	032	0.012	039	0.046	051	0.058
				017	0.064	025	0.064	033	0.022	040	0.067	052	0.076
				018	0.091	026	0.128	034	0.086	041	0.130	053	0.150
				019	0.122	027	0.179	035	0.162	042	0.159	054	0.258
				020	0.209	028	0.217	036	0.256	043	0.226		
				021	0.228	029	0.243						

Table 6 SDOF test (A1-2) PGA at bedrock

SDOF													
Sweep		Resweep		Northridge SM		Artificial		Northridge MW-CIT		Chuetsu		Kobe SM	
Event Number	PGA	Event Number	PGA	Event Number	PGA	Event Number	PGA	Event Number	PGA	Event Number	PGA	Event Number	PGA
001	0.012	004	0.014	007	0.011	014	0.0109	021	0.011	035	0.013	042	0.012
002	0.014	005	0.015	008	0.014	015	0.016	022	0.013	036	0.013	043	0.023
003	0.017	006	0.026	009	0.031	016	0.041	023	0.034	037	0.014	044	0.044
				010	0.064	017	0.064	024	0.065	038	0.034	045	0.077
				011	0.102	018	0.094	025	0.093	039	0.107	046	0.137
				012	0.146	019	0.130	026	0.115	040	0.181	047	0.198
				013	0.244	020	0.229	027	0.194	041	0.228	048	0.179
								028	0.207			049	0.186
								029	0.243			050	0.218
												051	0.232

Northridge-SM earthquake (Station: Santa Monica), 1995 Kobe-SM earthquake (Station: JMA Kobe), artificial seismic waves, 1994 Northridge earthquake (Station: CIT Seis Sta), and 2007 Chuetsu earthquake (Station: Iizuma Imokawa). The input motions were filtered from 20 to 300 Hz to comply with the allowable frequency range of the inflight shaking table, and the Northridge-SM and Kobe-SM were matched to the target spectrum according to KDS 17 10 00 (MLIT 2018, Nguyen *et al*. 2023). Time histories and response spectrums are plotted in Fig. 3.

The first test was free-field ground without structures (A1-1). After ramping up to the targeted centrifugal acceleration of 60 g, low-amplitude sweep and resweep motions were excited, and the first earthquake Kobe-SM was incrementally elevated from low amplitude (0.012 g) to 0.25 g level (see Table 5). Artificial seismic waves,

Table 2 2DOF test (A1-3) PGA at bedrock

2DOF													
Sweep		Resweep		Northridge SM		Kobe SM		Artificial		Northridge MW-CIT		Chuetsu	
Event Number	PGA	Event Number	PGA	Event Number	PGA	Event Number	PGA	Event Number	PGA	Event Number	PGA	Event Number	PGA
001	0.012	003	0.011	006	0.011	013	0.013	021	0.011	029	0.011	037	0.015
002	0.015	004	0.012	007	0.018	014	0.015	022	0.016	030	0.012	038	0.025
		005	0.023	008	0.045	015	0.041	023	0.038	031	0.014	039	0.043
				009	0.069	016	0.065	024	0.071	032	0.0297	040	0.077
				010	0.122	017	0.103	025	0.129	033	0.089	041	0.122
				011	0.207	018	0.107	026	0.218	034	0.129	042	0.191
				012	0.247	019	0.136	027	0.221	035	0.215	043	0.203
						020	0.278	028	0.234	036	0.281	044	0.212
												045	0.273

Table 3 3DOF test (A1-4) PGA at bedrock

3DOF													
Sweep		Resweep		Northridge SM		Kobe SM		Artificial		Northridge MW-CIT		Chuetsu	
Event Number	PGA	Event Number	PGA	Event Number	PGA	Event Number	PGA	Event Number	PGA	Event Number	PGA	Event Number	PGA
001	0.014	003	0.014	005	0.012	011	0.013	018	0.012	025	0.012	033	0.017
002	0.020	004	0.017	006	0.014	012	0.015	019	0.016	026	0.014	034	0.026
				007	0.032	013	0.039	020	0.036	027	0.015	035	0.045
				008	0.060	014	0.063	021	0.072	028	0.041	036	0.069
				009	0.102	015	0.104	022	0.128	029	0.113	037	0.125
				010	0.208	016	0.110	023	0.187	030	0.180	038	0.201
						017	0.203	024	0.251	031	0.220	039	0.196
										032	0.276	040	0.196
												041	0.217

Table 4 Test Information

Test ID	Structure Condition	Relative Density	Description
A1-1	N/A	77.10	Free field
A1-2	SDOF	78.23	SDOF Shallow foundation
A1-3	2DOF	79.96	2DOF Shallow foundation
A1-4	3DOF	80.45	3DOF Shallow foundation

Northridge-CIT, Chuetsu, and Northridge-SM earthquake records followed. Then, the ramping of the centrifuge was stopped after the first test was finished, and the SDOF structure was installed at 1 g and reaccelerated to 60 g for the next test. In tests with the structures, the excitation of the above-mentioned earthquakes were repeated (A1-2, Table 6). Further test series, A1-3 (2DOF structure; Table 7) and A1-4 (3DOF structure, Table 8) were repeated with the next structures replacements on the same soil model. The sequence of input motions and their peak ground acceleration (PGA) at the bedrock are tabulated in Tables 5 to 8. Due to repeated ramping up acceleration and seismic excitations, the model grounds were densified with a certain degree. The relative density for each test was re-evaluated by monitoring the surface settlement of the soil models during each test and the relative densities are tabulated in Table 9, indicating densification.

3. Results and discussion

3.1 Centrifuge test analysis results

In this study, the Northridge-SM ground motion was selected to represent the other input motions (Kobe SM, Artificial, Northridge-CIT, and Chuetsu) since this motion featured large-magnitude, and short-period earthquakes contents close to the natural periods of the tested structures, making it a suitable representative earthquake for comparative analysis. The time history accelerations measured by the accelerometers are processed to FDD, RS, and FFT.

The FDD method finally presents the cross spectral density functions (CPSD) and scale-factored mode shapes of each soil model and structure upon each earthquake

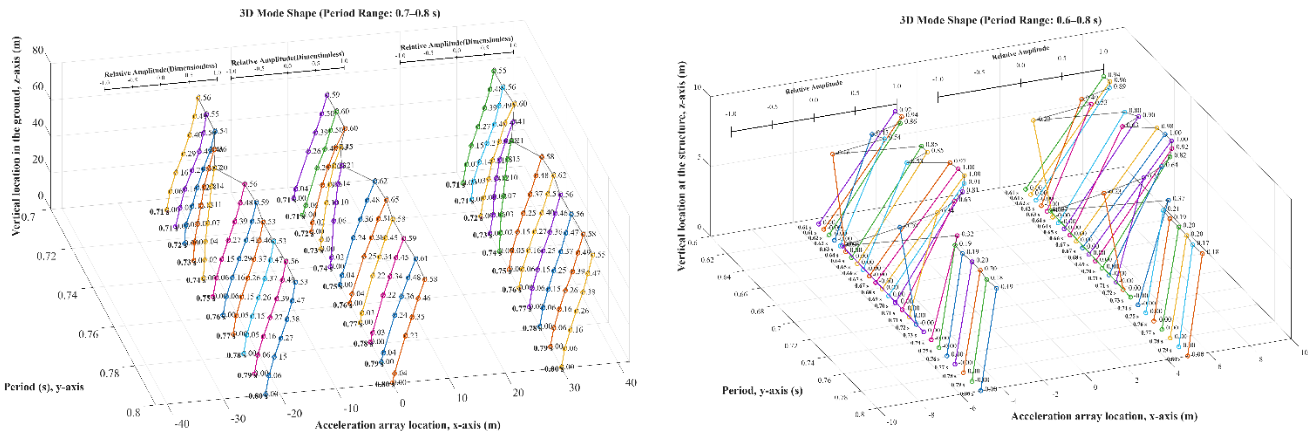

(a) ground (Test A1-2. Event 013)

(b) SDOF (Test A1-2. Event 013)

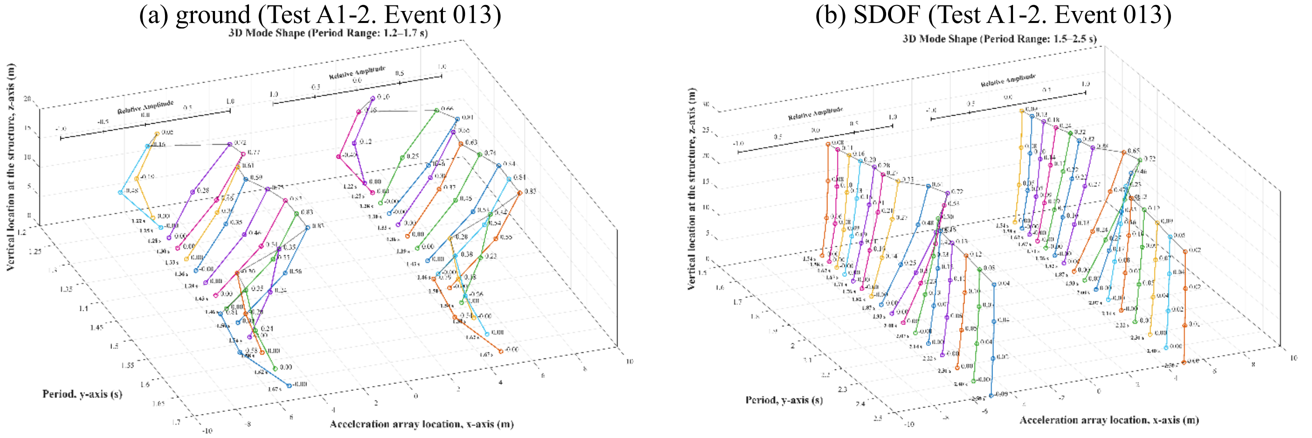

(c) 2DOF (Test A1-3. Event 012)

(d) 3DOF (Test A1-4. Event 010)

Fig. 4 Mode shapes of period band near the natural period by FDD using accelerations recorded Northridge-SM

event. Fig. 4 presents typical examples of the mode shapes for a period band (where the natural period is expected) in the extracted CPSD of each case with Northridge-SM. Fig. 4 shows typical examples of mode shapes for the predicted natural period bands from the extracted CPSDs for each case during the Northridge-SM. Fig. 4 illustrates the variation in mode shape amplitudes with periodic variation. Fig. 4(a) shows the FDD results for the ground (Test A1-2, Event 013), while Figs. 4(b)-4(d) show the FDD results for the SDOF, 2DOF, and 3DOF structures (Test A1-2, Event 013; Test A1-3, Event 012; Test A1-4, Event 010). The vertical axis (titled ‘vertical location in the ground, z-axis’ or ‘vertical location at the structure, z-axis’) indicates the height of the accelerometers embedded in the ground from the bedrock in Fig. 4(a), while Figs. 4(b)-4(d) show the vertical location of the accelerometers attached to each mass of the structure from the accelerometer attached to the foundation. The horizontal axis (x-axis), titled "Accelerometer array Location, x-axis" indicates the horizontal distance of the accelerometer array from the centerline of the ground model, with positive values in the south direction and negative values in the north direction along x-axis. In Fig. 4 and the FDD figures below, the markers represent the mode shape amplitudes of each accelerometer. Based on the horizontal inset axis titled "Relative Amplitude", southward motion is defined as positive, and northward motion is defined as negative, indicated by the numbers next to the markers. "Relative Amplitude" is defined as the component values of the eigenvectors derived through singular value decomposition (SVD), and represents the relative magnitude and phase relationship to the reference point (i.e., the bedrock or foundation in this paper), rather than the absolute magnitude, of the displacement response at each measurement location.

Therefore, the relative amplitude in the mode shape can be interpreted as a dimensionless index that intuitively represents the relative displacement distribution and vibration mode of each observed point positioned on the structure or ground. It can be seen that the mode shapes of both the ground and the structure are altered as its corresponding period changes, and the mode shape of the natural period (or the fundamental period) with the maximum relative amplitude is clearly observed at the specific period (which is expected as the natural period).

This is defined as the natural frequency and is compared to RRS and ratio of fast Fourier transform (RFFT). A single-degree-of-freedom of CPSD and mode shapes are plotted in Fig. 5. In Fig. 5(a), the period at which the maximum singular value is 0.76 s, and the mode shape of the ground can be identified at that period as shown in Fig. 5(c). At this time, the surface relative amplitude of the mode shape of the ground shows a maximum value at the ground period. In addition, CPSD of structure has two peaks (see Fig. 5(b)), which are the period of the ground (0.76 s) and the period of the structure (0.67 s), respectively.

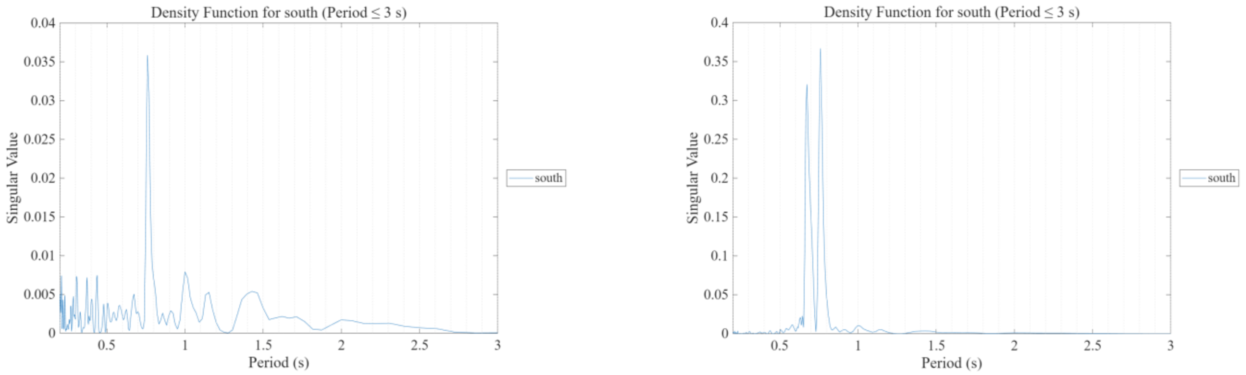

(a) CPSD of ground (b) CPSD of SDOF structure

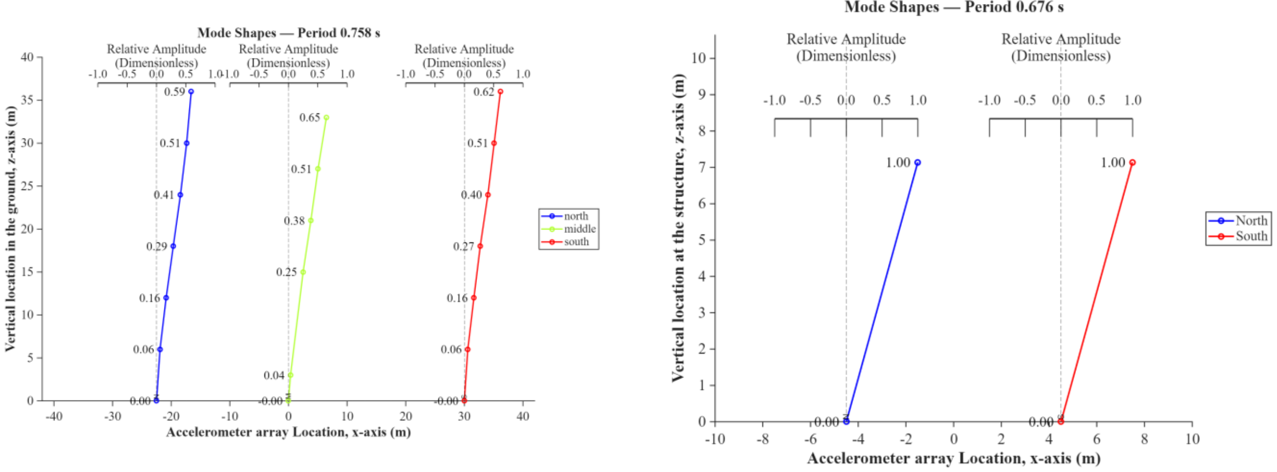

(c) mode shape of ground (d) mode shape of SDOF structure

Fig. 4 FDD results Test A1-2, Event 013, Northridge-SM

Additionally, enlarged figures of Fig. 4 are provided in Appendix Figs. A-1 to A-4.

The ground period is traditionally estimated by the ratio of the RS and FFT of the accelerometer embedded in the ground and the accelerometer attached to the bottom of the container (i.e. reference point), and the response of the structure to the ground period was observed by the ratio of the RS and FFT of the accelerometer of the structure mass and the accelerometer attached to the container. The ratio of response spectrum (RRS) and ratio of fast Fourier transform (RFFT) are defined using the measured motions from two different locations considered as the input and output of either ground or structure system as follows.

$$RRS = \frac{RS(each\ location)}{RS(Reference\ Point)} \tag{4}$$

$$RFFT = \frac{FFT(each\ location)}{FFT\ (Reference\ Point)} \tag{5}$$

A typical example of the RS, FFT, RRS, and RFFT of the ground and structure are plotted in Fig. 6. Fig. 6 compares the periods of the ground and structure calculated by the FDD with the red and blue dashed lines, respectively. The RSs and RRSs of the ground are plotted for each accelerometer at each depth. It can be seen that the RRSs are minimally affected by the frequency characteristics of input motions. The amplification becomes clearer at the natural period as the depth where the acceleration signals measured approaches the surface.

The period of the structure is also calculated from the ratio of the RS and FFT between the structure mass and foundation (reference point). In this study, the spectral density function and mode shapes of the extracted by FDD are then compared with the RS, RRS, FFT, and RFFT to find the periods of the ground and structure. The RRS of the structures and ground system (the solid line in Fig. 6) is calculated by dividing the RS of the mass by the average value of RS of the north and south bedrock (denoted as 'RRS_Mass1/BR' in Fig. 6), minimizing the influence of the input motion.

The RRS of the structures (the dashed line in Fig. 6) is calculated by dividing the RS of the mass by the average value of foundation (RRS_Mass1/FND), comparing to the RRS of the structure-ground system. The RS of the structure in Fig. 6(b) has two peaks (blue and red dotted lines), corresponding to both the natural periods of the ground and structure. The RRS of the structure-ground system ('RRS_Mass1/BR' the solid line in Fig. 6(d)) also has two amplifications at both the ground period of 0.76 s and the structure period of 0.67 s, even the influence of the input motion to the RRS is minimal. It is interesting to note that the RRS of the structure ('RRS_Mass1/ FND' the dashed line in Fig. 6(d)) presents the clearer amplification at

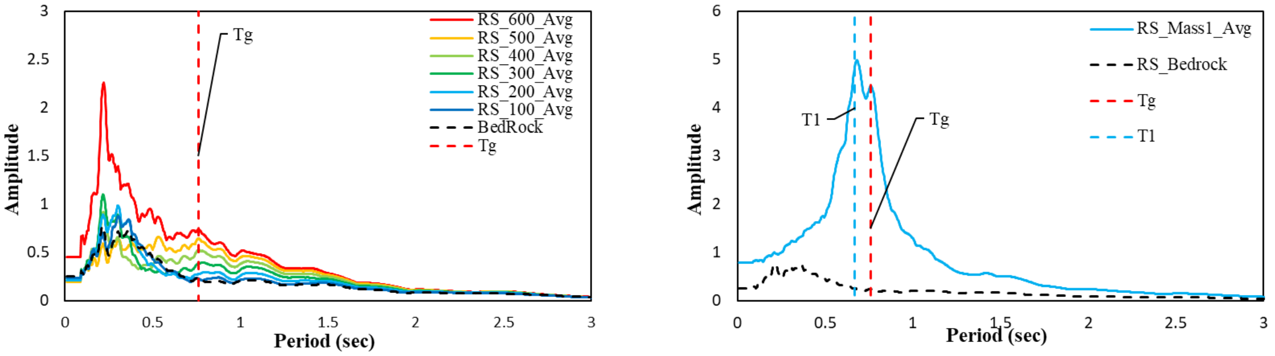

(a) RS of ground (b) RS of SDOF structure

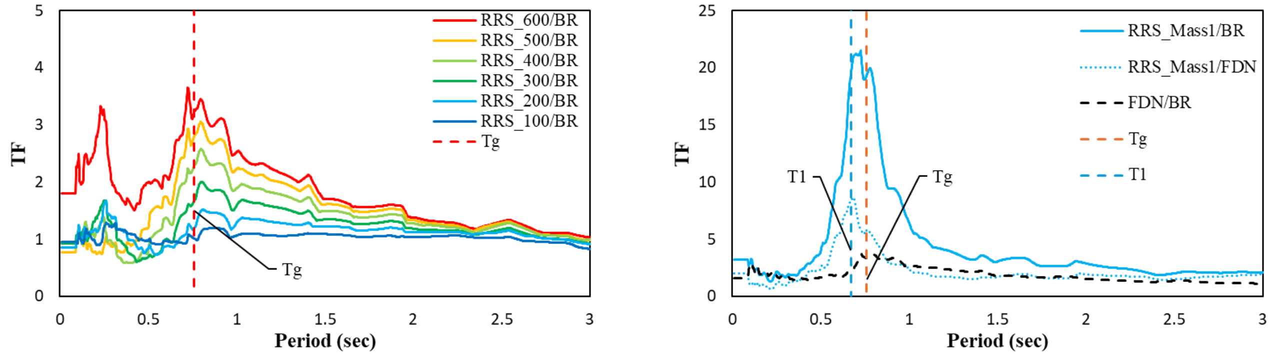

(c) RRS of ground (d) RRS of SDOF structure

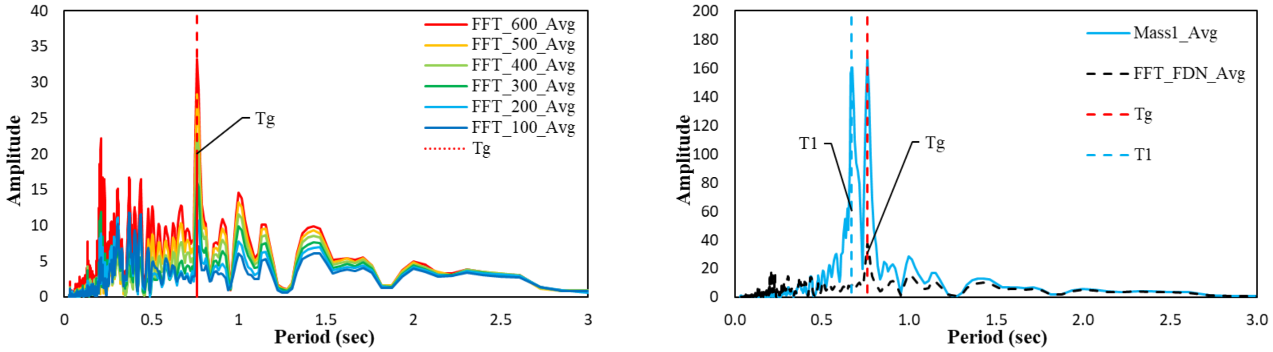

(e) FFT of ground (f) FFT of SDOF structure

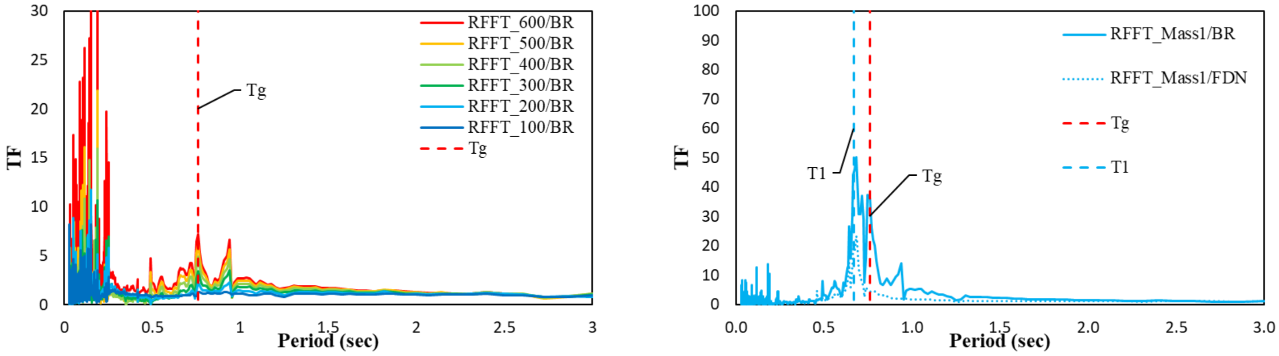

(g) RFFT of ground (h) RFFT of SDOF structure

Fig. 5 RS, RRS, FFT and RFFT of ground and SDOF structure Test A1-2, Event 013, Northridge-SM

the structure period (see Fig. 6(d)). Figs. A-5 to A-8 attached to the appendix show the results of SDOF structure tests, excluding Northridge-SM.

Figs. 7 and 8 shows the RS, RRS, CPSD, and mode shapes of a two-degree- and three-degree-of-freedom structures. In the ground CSPD of test A1-3, the period corresponding to the maximum singular value is 0.76 s (see Fig. 7(e)), and the maximum value of the relative amplitude can be seen at this peak (see Fig. 7(g)). In the case of the structure periods, corresponding to the peak and exhibiting

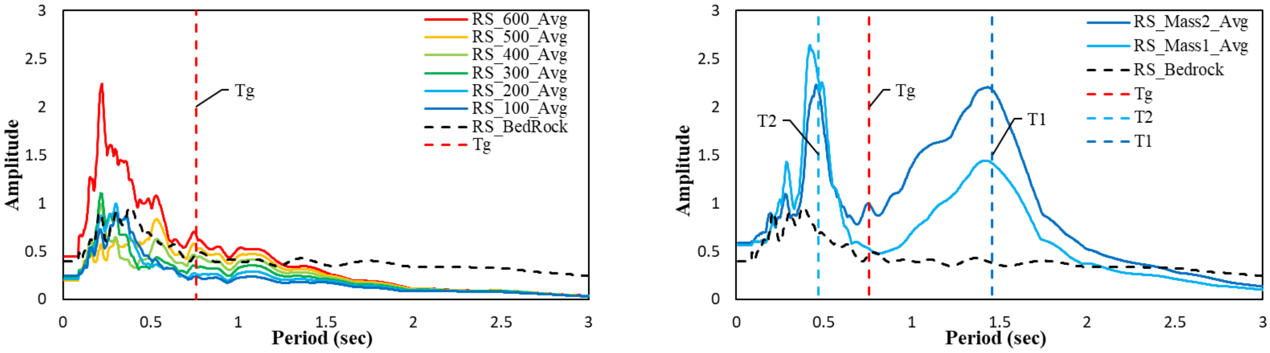

(a) RS of ground (b) RS of 2DOF structure

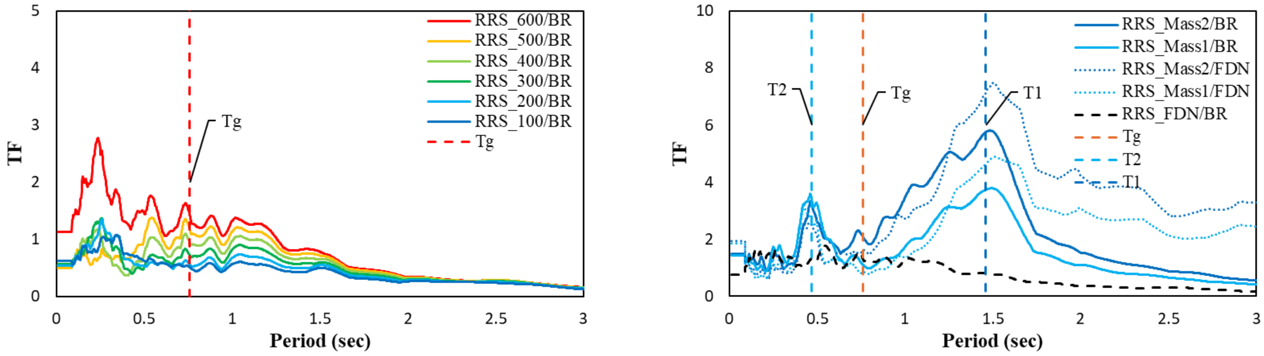

(c) RRS of ground (d) RRS of 2DOF structure

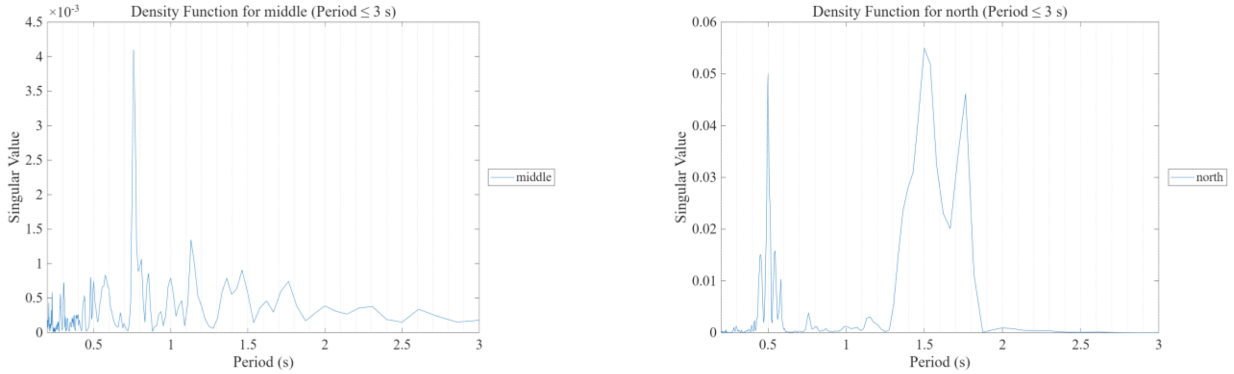

(e) CPSD of ground (f) CPSD of 2DOF structure

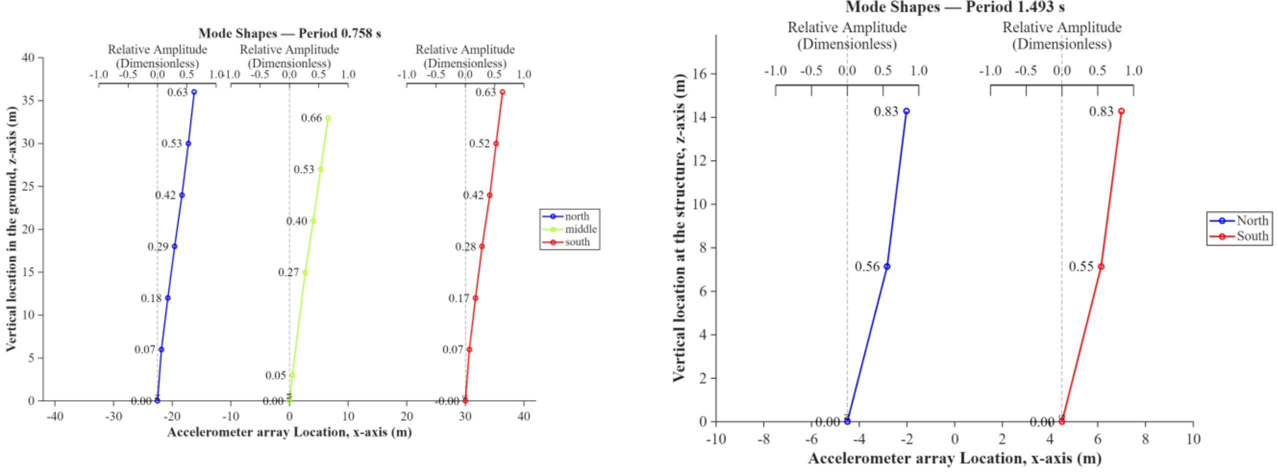

(g) mode shape of ground (h) mode shape of 2DOF structure

Fig. 6 RS, RRS, CPSD and mode shape of ground and 2DOF structure Test A1-3, Event 012, Northridge-SM

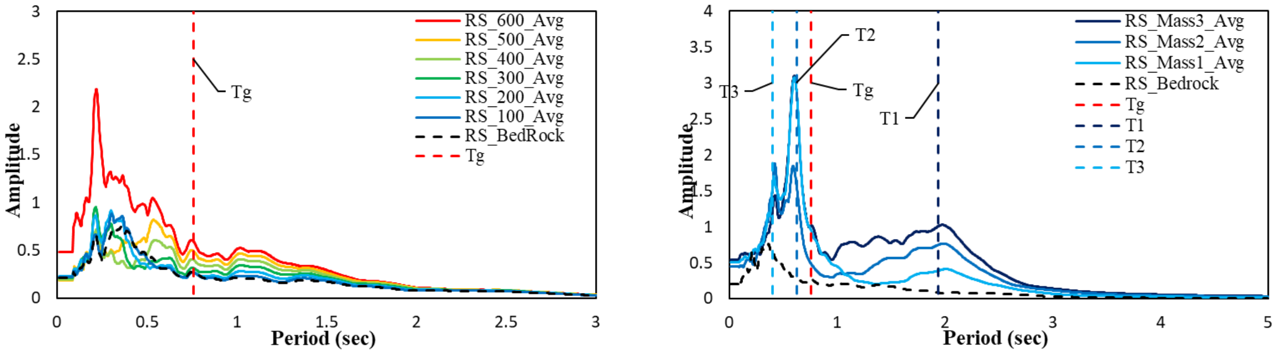

(a) RS of ground (b) RS of 3DOF structure

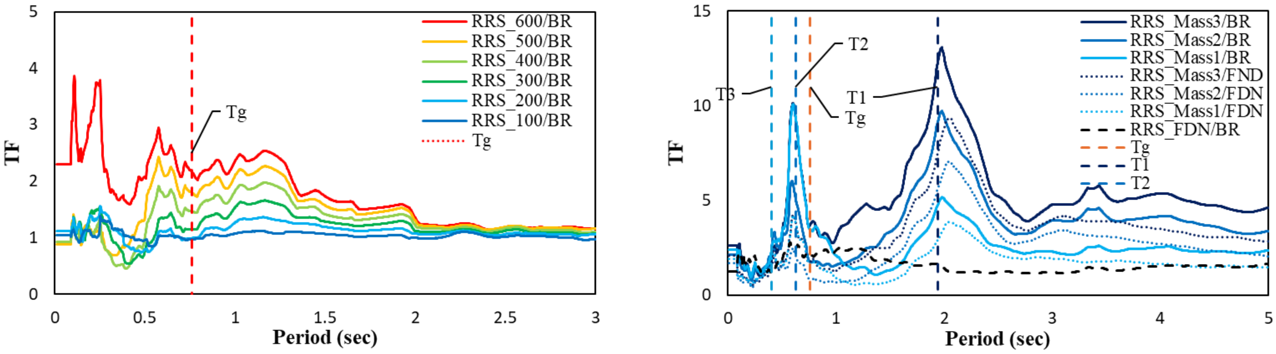

(c) RRS of ground (d) RRS of 3DOF structure

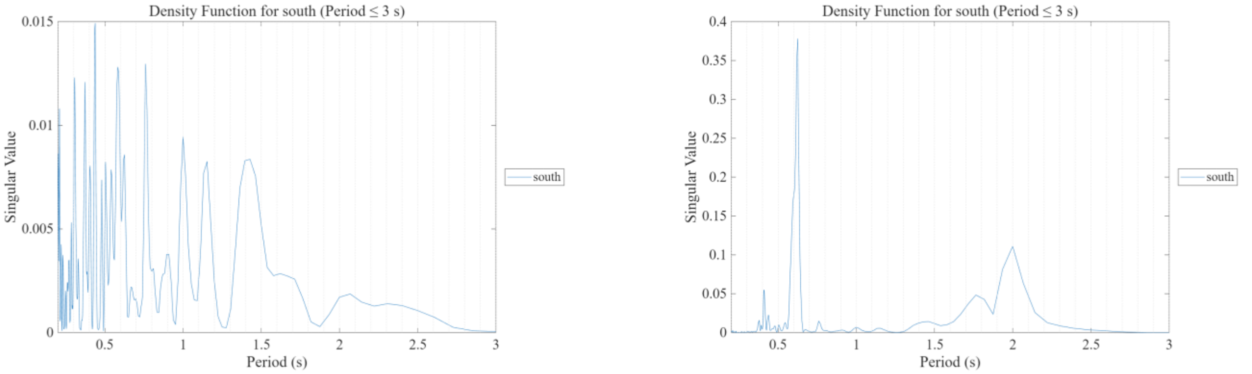

(e) CPSD of ground (f) CPSD of 3DOF structure

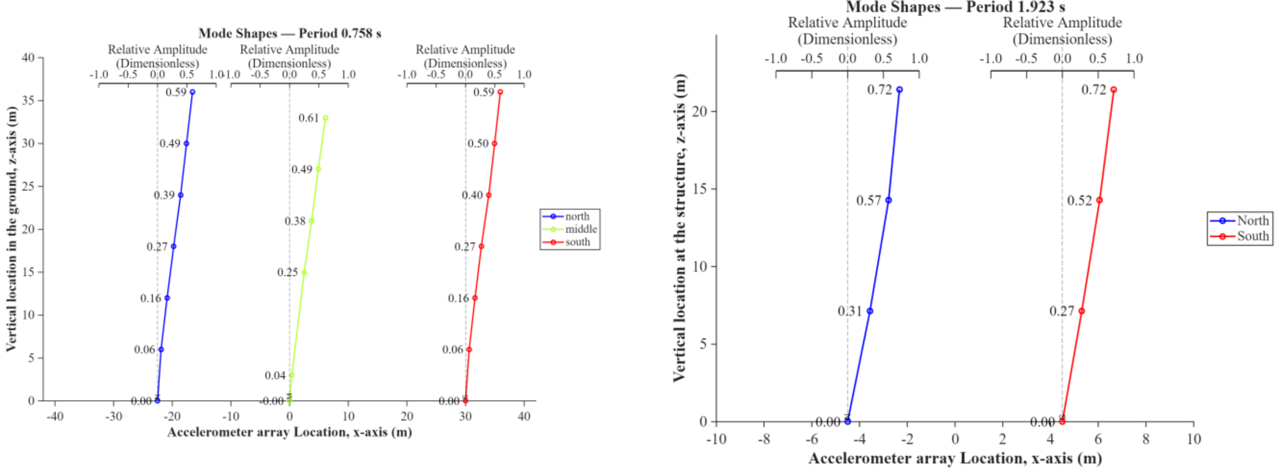

(g) mode shape of ground (h) mode shape of 3DOF structure

Fig. 7 RS, RRS, CPSD and mode shape of ground and 3DOF structure Test A1-4, Event 010, Northridge-SM

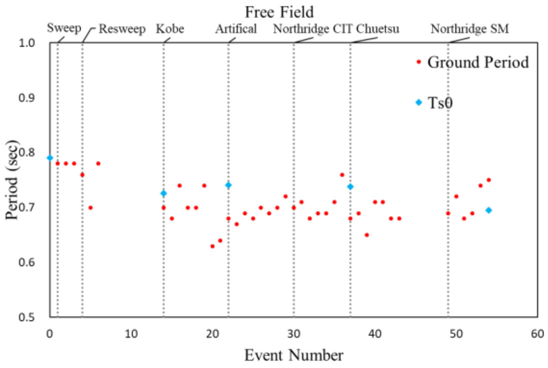

(a) ground period of Test A1-1

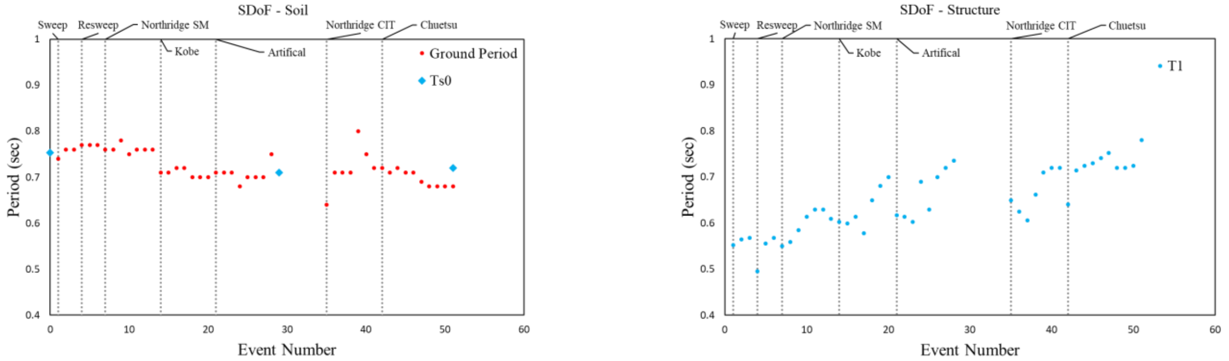

(b) ground period of Test A1-2

(c) lengthened SDOF structure period of Test A1-2

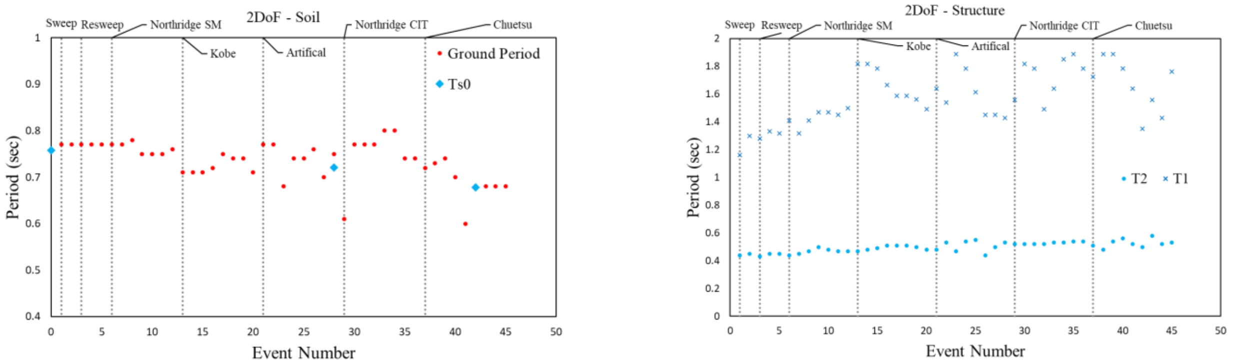

(d) ground period of Test A1-3

(e) lengthened 2DOF structure period of Test A1-3

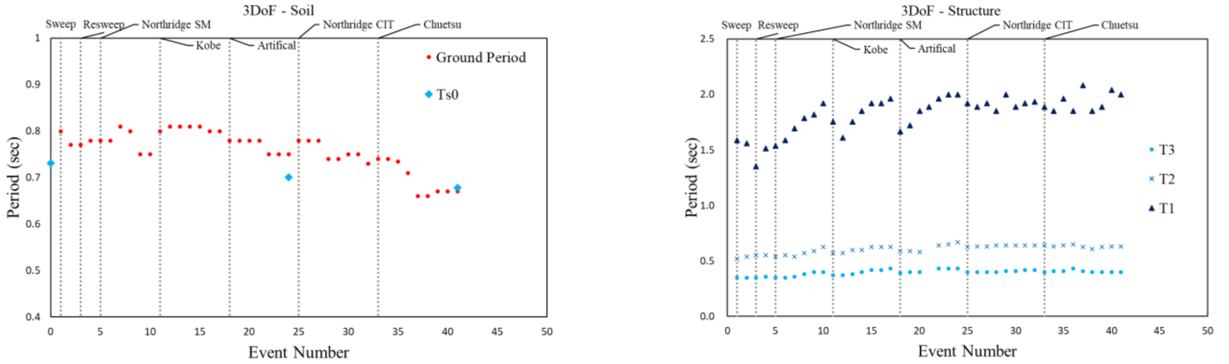

(f) ground period of Test A1-4

(g) lengthened 3DOF structure period of Test A1-4

Fig. 8 Ground and lengthened structure period

the maximum value of relative amplitude was taken as the lengthened natural period of the structure, which indicates the natural mode shape of the structure (see Figs. 7(f) and 7(h)). Thus two-degree-of-freedom structure has two periods of 1.49 s and 0.47 s. Figs. A-9 to A-12 show the results of the 2DOF structure tests for the other earthquake excitation, excluding Northridge-SM.

And the three-degree-of-freedom structure has three periods of 1.92 s, 0.63 s, and 0.4 s (Fig. 8). Some of the structure periods are much closer to the natural period band of the ground, so that it is difficult to identify each period of each component. In particular, All of the RS, RRS, and CPSD of the ground, where the three-degree-of-freedom structure is installed, sometimes calculates various multiple peaks in various frequency bands (see Fig. 8(c)), interfering clear identification of the periods of the structure and ground. Interestingly, the relative amplitude is maximized at the natural period of the ground, indicating the mode shape of the ground. All three periods of the three-degree-of-freedom structure are successfully interpreted from the structure's spectral density functions and mode shapes. Figs. A-13 to A-16 show the results of three-degree-of-freedom structure tests for the other input motions, excluding Northridge-SM, and the results are consistent. The mode shapes extracted by the FDD successfully complements RS, FFT, RRS, and RFFT to calculate and identify the lengthened natural periods of multi-degree-of-freedom structures among multiple peaks. Additionally, the FDD's unique mode shape, which indicates the maximum relative amplitude at the natural period, can clearly prove that the identified period is the natural period.

3.2 Period lengthening

Fig. 9 plots the periods of the ground and structure calculated by the FDD method for all earthquake excitation events and dotted line is presented first event each earthquake. The blue rhombus represents the ground period (T_{s0}) calculated from the shear wave velocity measured by the bender element using Eq. (6). In Fig. 9, T_{s0} is similar to the ground period, which demonstrates the high accuracy of the ground period calculated by the FDD method.

$$T_{s0} = 4H/V_s \tag{6}$$

Where, T_{s0} is ground period, H is ground specimen height (=36 m in prototype) and V_s is average shear velocity of the entire soil layer.

At the early excitations with weak PGA, the natural period of the ground partly shows a decreasing trend as the event number increases. It can be explained that the decrease in the ground period is attributed to the densification of the ground due to centrifugal acceleration and successive excitations as the event number increases. But the ground period of some events is increasing when the intensity (PGA) increases. It seems that increasing PGA for each earthquake makes the periods of the soil increase due to more severe nonlinearity. The ground periods measured by the bender element tests are plotted together in Fig. 9, confirming the consistency of the FDD results with the bender element measurements. In general, sandy granular material tends to become denser with cyclic loading. On the other hand, if the ground becomes denser, the period of the structure is supposed to decrease due to increased stiffness. However, it is observed that the lengthened natural period of the structure in this study tends to increase with the event number. It can be inferred that the period-lengthening effect (i.e., the SFSI effect) becomes more pronounced because of severe soil non-linearity at shallow depths, induced by the rotation of the structure with increasing ground accelerations, as well as by sliding, uplifting, and separation between the soil and the structure during previous events, which reduce the strength of the soil–structure interface. In addition, the translation and rocking modes of the structures are altered with different structures, causing this inconsistent trend in the structural periods.

4. Conclusions

In this study, a series of dynamic centrifuge tests were conducted on single-, two-, and three-degree-of-freedom structures installed on shallow foundations and sandy ground. The frequency domain decomposition method was newly applied to discriminate the periods of structures and ground by comparing RS, RRS, FFT, and RFFT.

- The mode shapes at their corresponding natural frequencies of the ground and structures are effectively calculated using the frequency domain decomposition method. The ground period observed by the FDD method is amplified and well matched to the results of the RRS and RFFT in terms of the natural periods. Especially, those results of FDD, RRS, and RFFT are well aligned to the natural periods calculated from shear wave velocity measured by bender element tests, indicating high reliability.
- The frequency domain decomposition method is capable of identifying the periods of all components (including soil, foundation, and MDOF structures) in the combined complex system with confirming the mode shapes at the corresponding periods of the components. Under such the conditions, the dynamic responses of the ground and structure interfere with each other, presenting multiple peaks in their frequency domain at each period of the ground and structure. The calculated ground and structure periods showed similar periods to the results of RS, RRS, FFT, and RFFT.
- RS, FFT, RRS, and RFFT identifying the period only based on the maximum amplitude, which can lead to the mis-selection of period among multi-peak conditions contributed by the interaction between many components in a dynamic system. In contrast, mode shapes extracted by FDD method, which are unique characteristics, enabling more precise period identification based on maximum relative amplitudes within the natural period range able to evidence that 'the identified period is the natural period'.
- In this study, as the number of earthquake excitations increases, the ground period tends to decrease to a certain level due to the possible compaction of the sandy ground. On the other hand, even though the ground period decreases, the lengthened periods of the structures is not consistent. When seismic loads are repeated and their magnitude gradually increases, the ground surface strain increases and the foundation-soil stiffness decreases. Therefore, it is presumed that the nonlinearity of the subgrade during earthquakes, significantly lengthens the period due to soil-structure interaction.
- In seismic design practice, especially for shallow

foundations, the stiffness of the foundation and soil significantly influence the dynamic characteristics (e.g., period) of the structure. ASCE 7-22 and NIST emphasized the importance of considering soil-foundation-structure interaction in the seismic design, and specifically proposed equations that account for the nonlinear effects of the soil. These equations include lengthened periods (structure period of interacting with the soil). Further research is required to extend the current finding to derive practical procedures to evaluate period lengthened for various soil and structure conditions.

- Additionally, this study only tackles the period lengthening effect, but since the period lengthening of a structure according to excitation is affected not only by the stiffness of the soil-foundation interface but also by the dynamic behavior (rotation, translation) of the structure, future research is required that separates the rotation and translation behavior of the structure."

Acknowledgments

This work was supported by the National Research Foundation of Korea (NRF) grant funded by the Korea government (MSIT) (No. RS-2024-00406320). This work was supported by the research grant of Kongju National University in 2025.

References

Alshawmar, F. and Fall, M. (2021), "Dynamic response of thickened tailings in shaking table testing", *Int. J. Geo-Eng.*, **12**(1), 28. https://doi.org/10.1186/s40703-021-00156-1.

American Society of Civil Engineers (2021), "Minimum design loads and associated criteria for buildings and other structures", Reston, VA: American Society of Civil Engineers.

Bendat, J.S. and Piersol, A.G. (1986), "Random data: Analysis and measurement procedures", John Wiley & Sons.

Brincker, R., Zhang, L. and Andersen, P. (2000), "Modal identification from ambient responses using frequency domain decomposition", *Proceedings of the IMAC 18 International Modal Analysis Conference (IMAC),* San Antonio, Texas, USA, February 7-10, 2000. 625-630, The International Modal Analysis Conference, San Antonio, Texas, United States, 07/02/2000.

Chaudhary, K., Shrestha, K.C. and Acharya, O. (2023), "Vulnerability assessment of residential steel building considering soil structure interaction", *Earthq. Struct.*, **25**(2), 79-87. https://doi.org/10.12989/eas.2023.25.2.079.

Deviprasad, B.S. and Dodagoudar, G.R. (2020), "Seismic response of bridge pier supported on rocking shallow foundation", *Geomech. Eng.*, **21**(1), 73-84. https://doi.org/10.12989/gae.2020.21.1.073.

Falcon, S.S.D. (2024), "Centrifuge modeling of seismic response of soil-foundation-building systems supported by shallow foundationsand deep basements", Ph.D. Dissertation, Kongju National University, Korea.

Freeman, S.A. (2007), "Response spectra as a useful design and analysis tool for practicing structural engineers", *ISET J. Earthq. Technol.*, **44**(1), 25-37.

Gillis, K.M. (2015), "Seismic response of shallow underground structures in dense urban environments", Ph.D. Dissertation, University of Colorado, Boulder.

Hadianfard, M.A. and Kamali, S. (2020), "Analysis of modal frequencies estimated from frequency domain decomposition method", *Int. J. Eng. Technol.*, **12**(3), 41-47. https://doi.org/10.7763/IJET.2020.V12.1182.

Hızal, Ç. (2023), "FDD based modal identification of structures using least squares approach", *Structures*, **55**, 1071-1083. https://doi.org/10.1016/j.istruc.2023.06.092.

Hızal, Ç. and Gül, B.K. (2025), "Assessing uncertainty bounds in frequency domain decomposition", *J. Civil Struct. Health Monit*, **15**, 2119-2138. https://doi.org/10.1007/s13349-025-00932-y.

Hu, L., Zhen, Z., Wang, F., Qiu, G., Li, Y., Shafie-khah, M. and Catalão, J.P. (2020), "Ultra-short-term solar PV power forecasting method based on frequency-domain decomposition and deep learning", *In 2020 IEEE Industry Applications Society Annual Meeting*, 1-8. IEEE. https://doi.org/10.1109/IAS44978.2020.9334889.

Iiyama, K., Morikawa, H., Chen, P.Y. and Sakai, K. (2024), "Analytical discussion on applicability of frequency domain decomposition method to systems excited by an impulse force", *J. Civil Eng. Management*, **30**(5), 452-464. https://doi.org/10.3846/jcem.2024.21347.

Jawalageri, S., Prendergast, L.J., Jalilvand, S. and Malekjafarian, A. (2022), "Effect of scour erosion on mode shapes of a 5 MW monopile-supported offshore wind turbine", *Ocean Eng.*, **266**, 113131. https://doi.org/10.1016/j.oceaneng.2022.113131.

Kiani, K. and Emami, S.M.M. (2024), "The effect of infill walls on the fundamental period of steel frames by considering soil-structure interaction", *Earthq. Struct.*, **26**(6), 417-431. https://doi.org/10.12989/eas.2024.26.6.417.

Kim, D.K., Lee, S.H., Kim, D.S., Choo, Y.W. and Park, H.G. (2015), "Rocking effect of a mat foundation on the earthquake response of structures", *J. Geotech. Geoenviron. Eng.*, **141**(1), 04014085. https://doi.org/10.1061/(ASCE)GT.1943-5606.0001207.

Kim, D.S., Kim, N.R., Choo, Y.W. and Cho, G.C. (2012), "A Newly Developed state-of-the-art Geotechnical Centrifuge in Korea", *KSCE J. Civil Eng.*, **17**(1), 77-84. https://doi.org/10.1007/s12205-013-1350-5

Ko, K.W., Ha, J.G., Park, H.J. and Kim, D.S. (2019), "Investigation of period-lengthening ratio for single-degree-of-freedom structures using dynamic centrifuge test", *J. Earthq. Eng.*, **25**(7), 1358-1380. https://doi.org/10.1080/13632469.2019.1576557.

Kumar, S., Choudhary, S.S. and Burman, A. (2024), "Machine induced dynamic field responses of group pile with different pile arrangements", *Int. J. Geo-Eng.*, **15**(1). https://doi.org/10.1186/s40703-024-00207-3.

Lee, S.H., Choo, Y.W. and Kim, D.S. (2013), "Performance of an Equivalent Shear Beam (ESB) model container for dynamic geotechnical centrifuge tests", *Soil Dynam. Earthq. Eng.*, **44**, 102-114. https://doi.org/10.1016/j.soildyn.2012.09.008.

Lv, Y., Yang, J., Li, F. and Liu, P. (2025), "Seismic responses analysis of rigid frame bridges with footing uplift considering soil-structure interaction", *Earthq. Struct.*, **28**(3), 265-278. https://doi.org/10.12989/eas.2025.28.3.265.

Ministry of Land, Infrastructure and Transport (MLIT) (2018), General seismic design (KDS 17 10 00). Ministry of Land, Infrastructure and Transport, Korea.

Mostafaei, Y. and Soleimani Kutanaei, S. (2025), "Modeling and prediction of embankment dam displacement under earthquake loading using artificial neural networks and swarm optimization algorithm", *Int. J. Geo-Eng.*, **16**(1). https://doi.org/10.1186/s40703-025-00235-7.

Nagula, S.S., Hwang, Y.W., Dashti, S. and Grabe, J. (2021), "Seismic site response of layered saturated sand: comparison of finite element simulations with centrifuge test results", *Int. J. Geo-Eng.*, **12**(1), 26. https://doi.org/10.1186/s40703-021-00155-2.

Nguyen, A.D., Nguyen, V.T. and Kim, Y.S. (2023), "Finite element analysis on dynamic behavior of sheet pile quay wall dredged and improved seaside subsoil using cement deep mixing", *Int. J. Geo-Eng.*, **14**(1). https://doi.org/10.1186/s40703-023-00186-x.

NIST, N. (2012), Soil-structure-interaction for building structures (nist gcr 12-917-21). National Institute of Standards and Technology, Gaithersburg, MD, 20899.

Qu, C.X., Liu, Y.F., Yi, T.H. and Li, H.N. (2023), "Structural damping ratio identification through iterative frequency domain decomposition", *J. Struct. Eng.*, **149**(5), 04023042. https://doi.org/10.1061/JSENDH.STENG-11837.

Soralump, S., Panthi, K., Nuannin, P. and Ornthammarath, T. (2025), "Seismic damage of high-rise buildings in Bangkok caused by soft soil amplification from Mw 6.4 Laos earthquake", *Earthq. Struct.*, **28**(6), 469-477. https://doi.org/10.12989/eas.2025.28.6.469.

Stringer, M., Heron, C. and Madabhushi, S. (2010), "Experience using MEMS-based accelerometers in dynamic testing. In: (Eds., S. Springman, J. Laue and L. Seward)", *Physical Modelling in Geotechnics*, Two Volume Set. CRC Press.

Teymur, B. and Madabhushi, S.P.G. (2003), "Experimental study of boundary effects in dynamic centrifuge modelling", *Géotechnique*, **53**(7), 655-663. https://doi.org/10.1680/geot.2003.53.7.655.

Veletsos, A.S. and Meek, J.W. (1974), "Dynamic behaviour of building-foundation systems", *Earthq. Eng. Struct. D.*, **3**(2), 121-138. https://doi.org/10.1002/eqe.4290030203.

Vucetic, M. and Dobry, R. (1987), "Dynamic properties and seismic response of soft clay deposits", *Proceedings of the International Symposium on Geotechnical Engineering of Soft Soils*, 51-87.

Youn, J.U., Choo, Y.W. and Kim, D.S. (2008), "Measurement of small-strain shear modulus Gmax of dry and saturated sands by bender element, resonant column, and torsional shear tests", *Can. Geotech. J.*, **45**(10), 1426-1438. https://doi.org/10.1139/T08-069.

Yun, J.S., Park, S.J., Falcon, S.S., Han, J.T., Kim, D. and Choo, Y.W. (2024), "Seismic response of braced excavation wall supporting deep sand layer using dynamic centrifuge tests", *Soil Dyn. Earthq. Eng.*, **183**, 108782-108782. https://doi.org/10.1016/j.soildyn.2024.108782.

Yun, J.W. and Han, J.T. (2021), "Dynamic behavior of pile-supported wharves by slope failure during earthquake via centrifuge tests", *Int. J. Geo-Eng.*, **12**(1), 33. https://doi.org/10.1186/s40703-021-00161-4.

Zeng, X. and Schofield, A.N. (1996), "Design and performance of an equivalent-shear-beam container for earthquake centrifuge mModelling", *Geotechnique*, **46**(1), 83-102. https://doi.org/10.1680/geot.1996.46.1.83.

IC

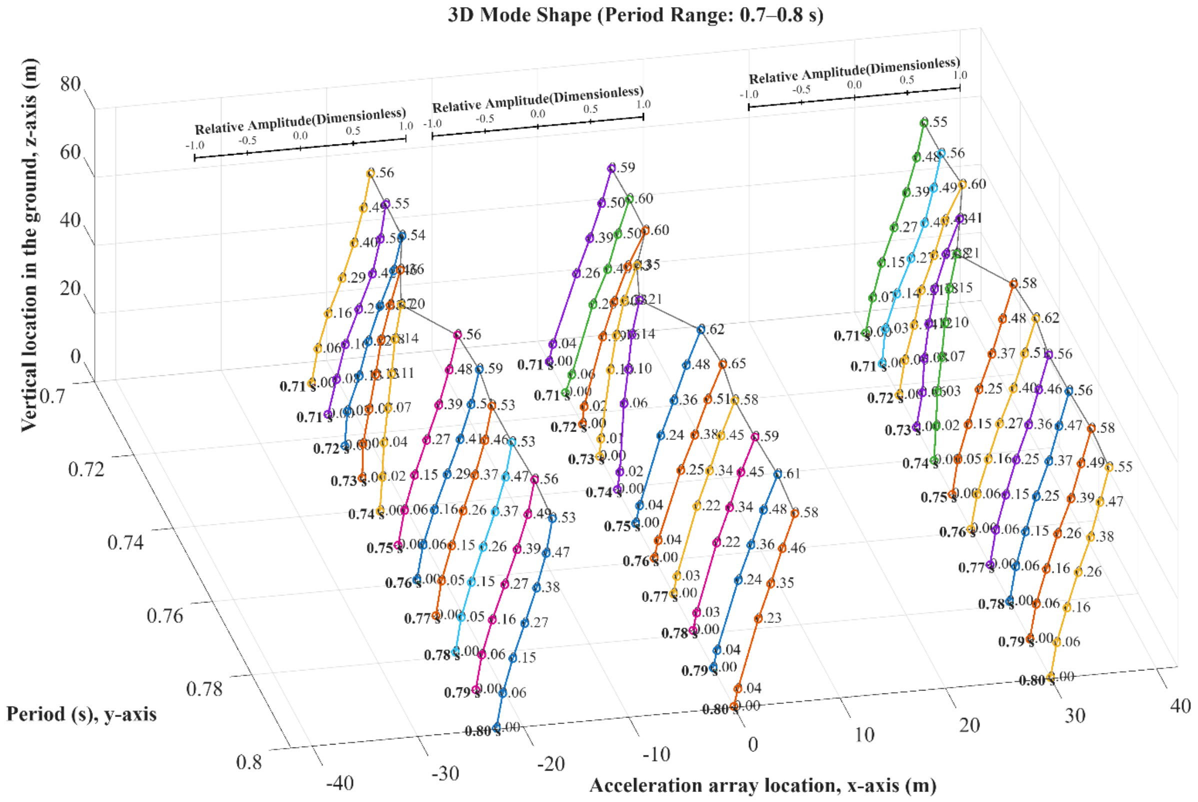

Fig. A-1Ground mode shapes of period band near the natural period by FDD (Test A1-2. Event 013)

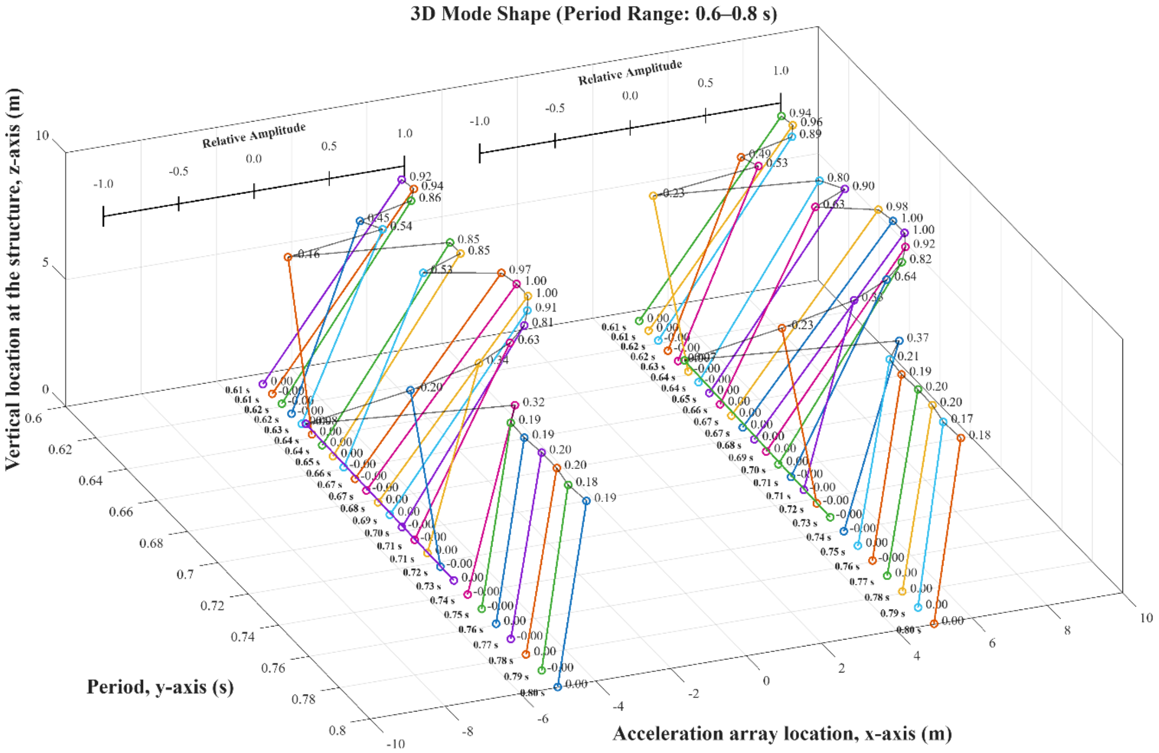

Fig. A-2 SDOF mode shapes of period band near the natural period by FDD (Test A1-2. Event 013)

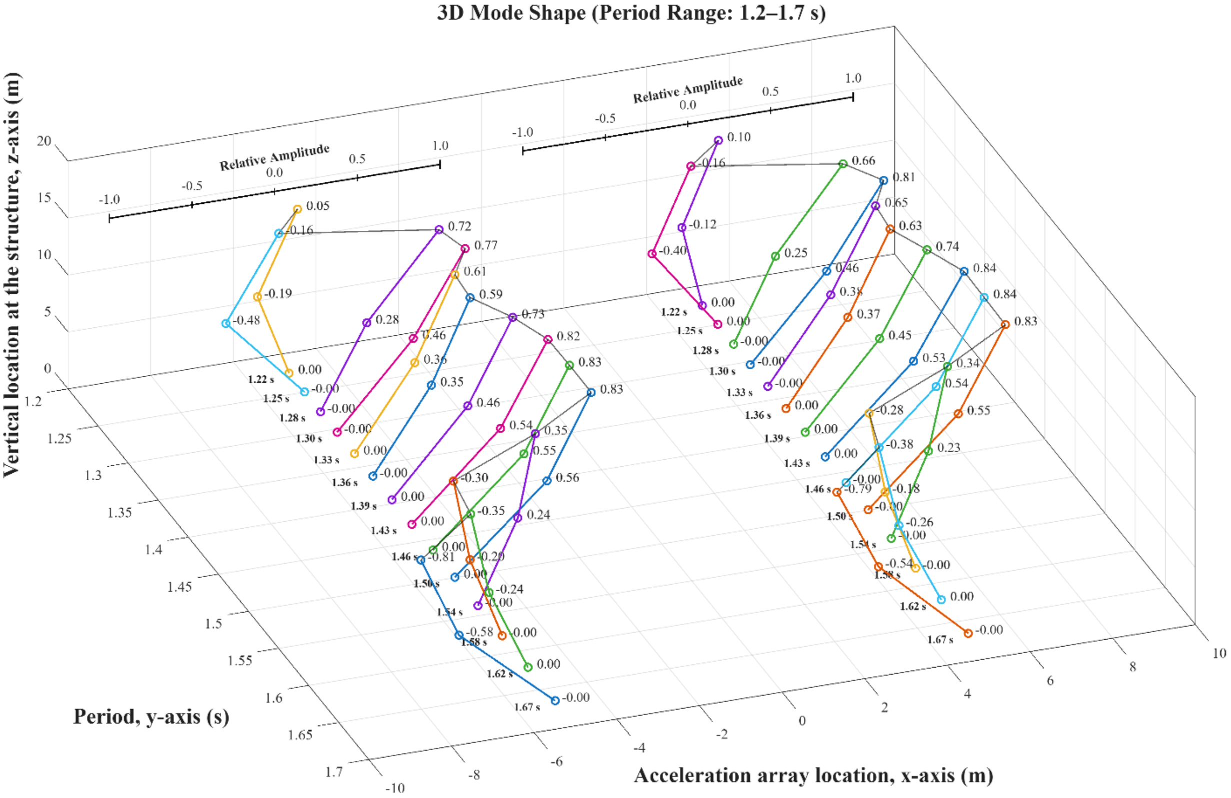

Fig. A-3 2DOF mode shapes of period band near the natural period by FDD (Test A1-3. Event 012)

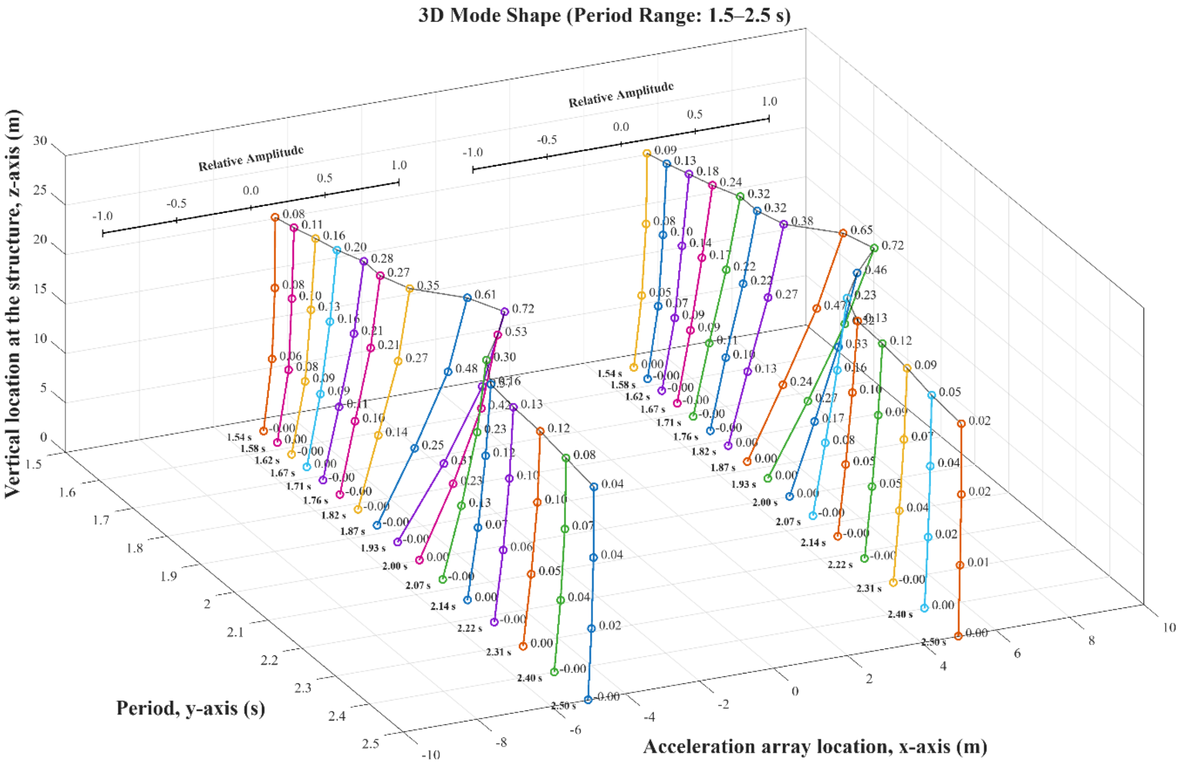

Fig. A-4 3DOF mode shapes of period band near the natural period by FDD (Test A1-4. Event 010)

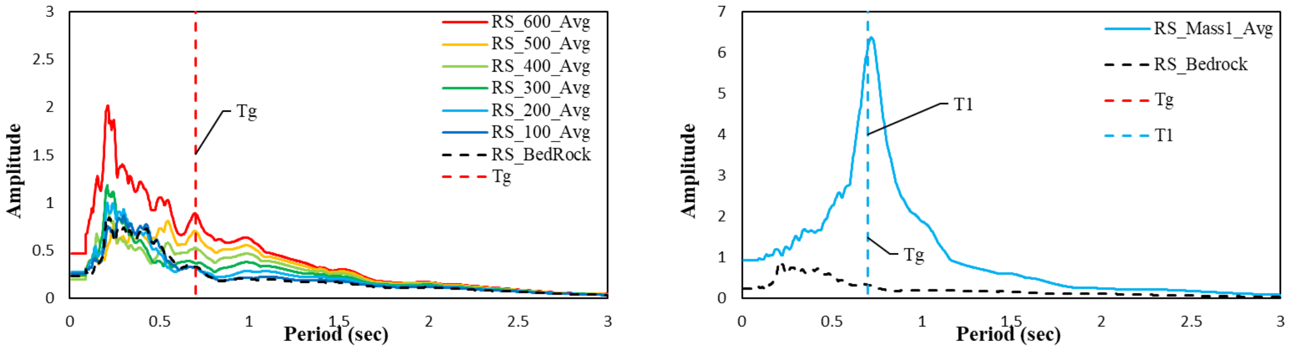

(a) RS of ground (b) RS of SDOF structure

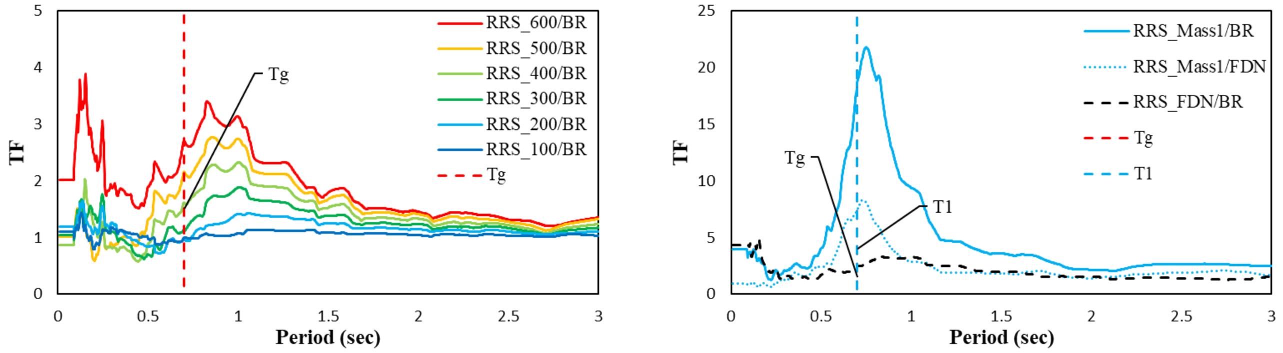

(c) RRS of ground (d) RRS of SDOF structure

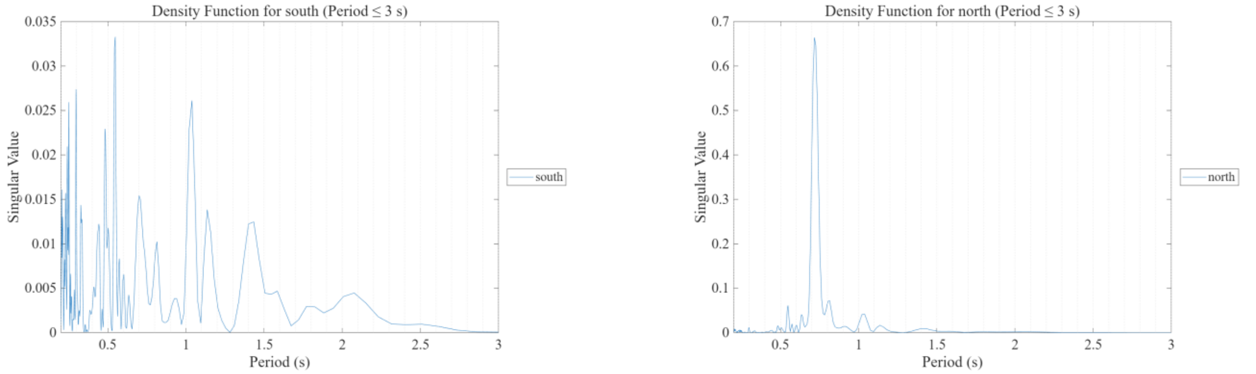

(e) CPSD of ground (f) CPSD of SDOF structure

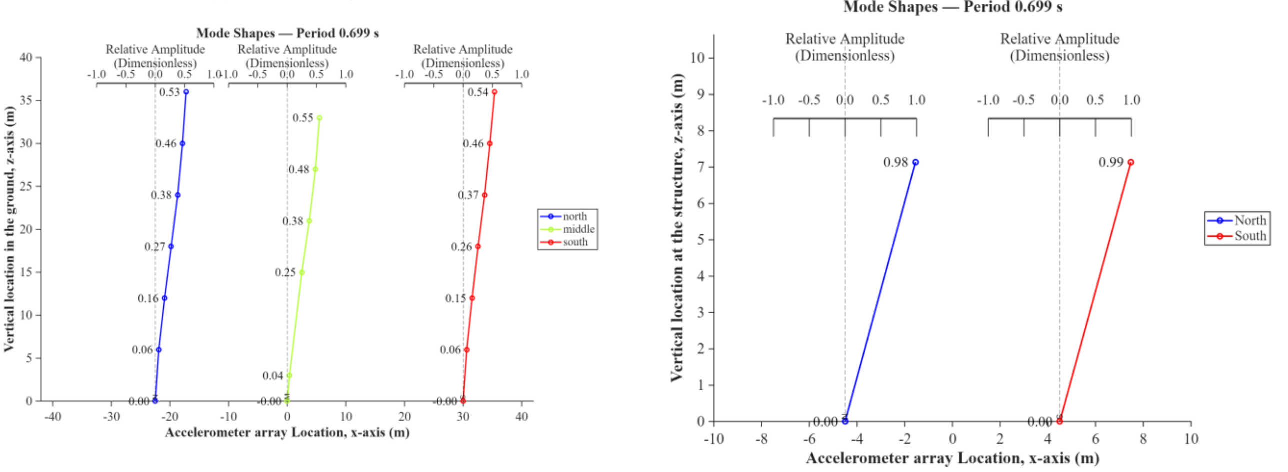

(g) mode shape of ground (h) mode shape of SDOF structure

Fig. A-5 RS, RRS, CPSD and mode shape of ground and SDOF structure Test A1-2, Event 020, Kobe-SM

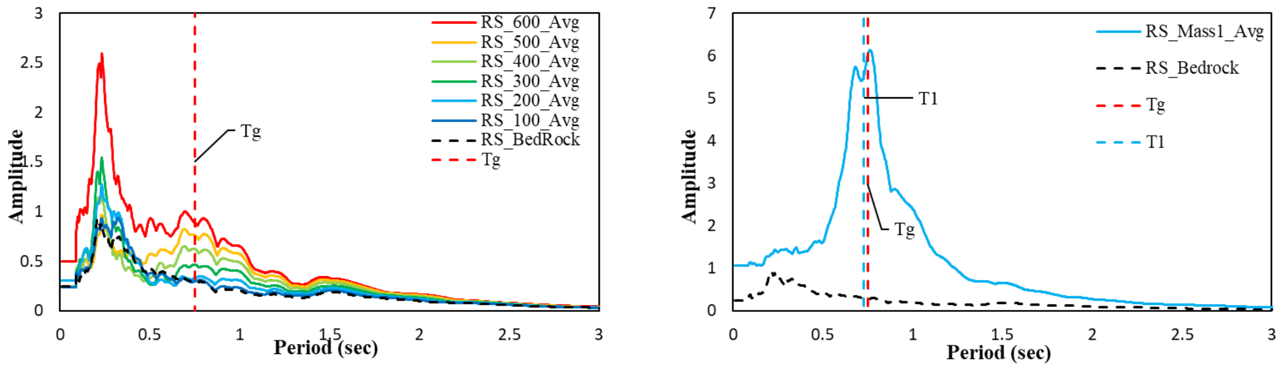

(a) RS of ground (b) RS of SDOF structure

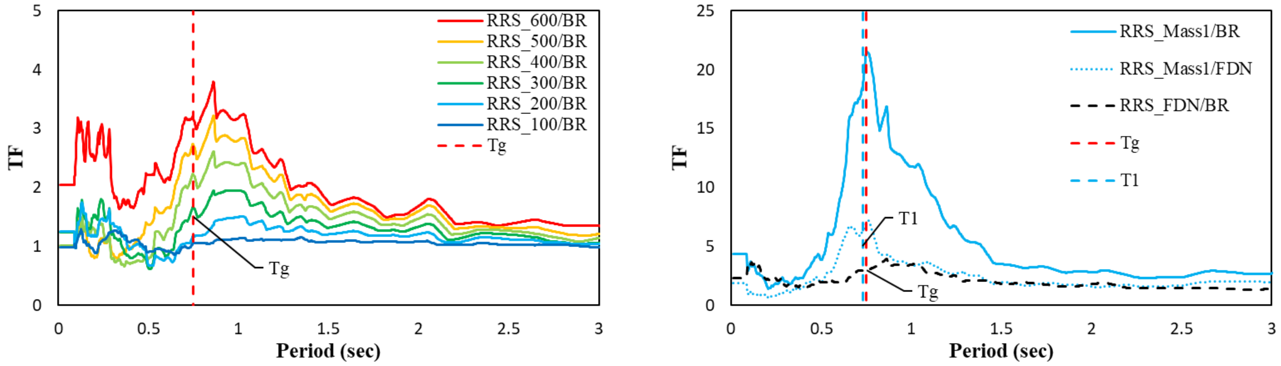

(c) RRS of ground (d) RRS of SDOF structure

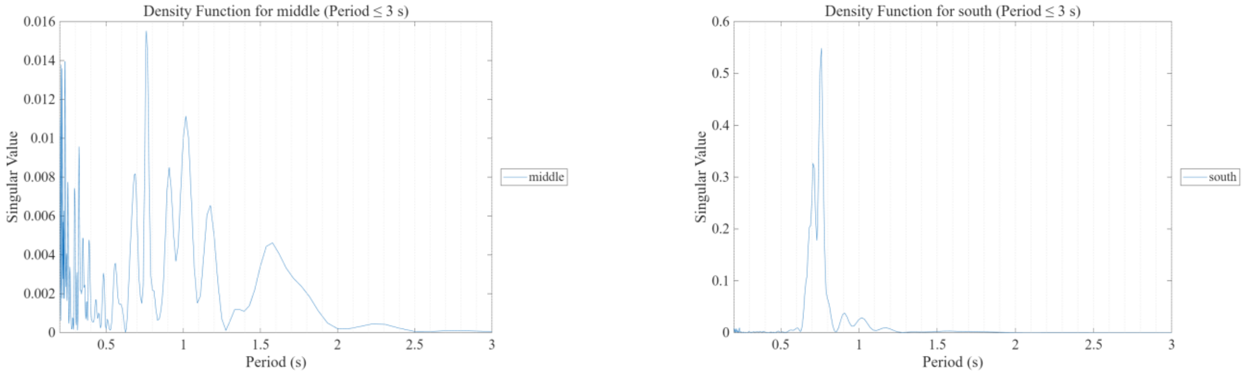

(e) CPSD of ground (f) CPSD of SDOF structure

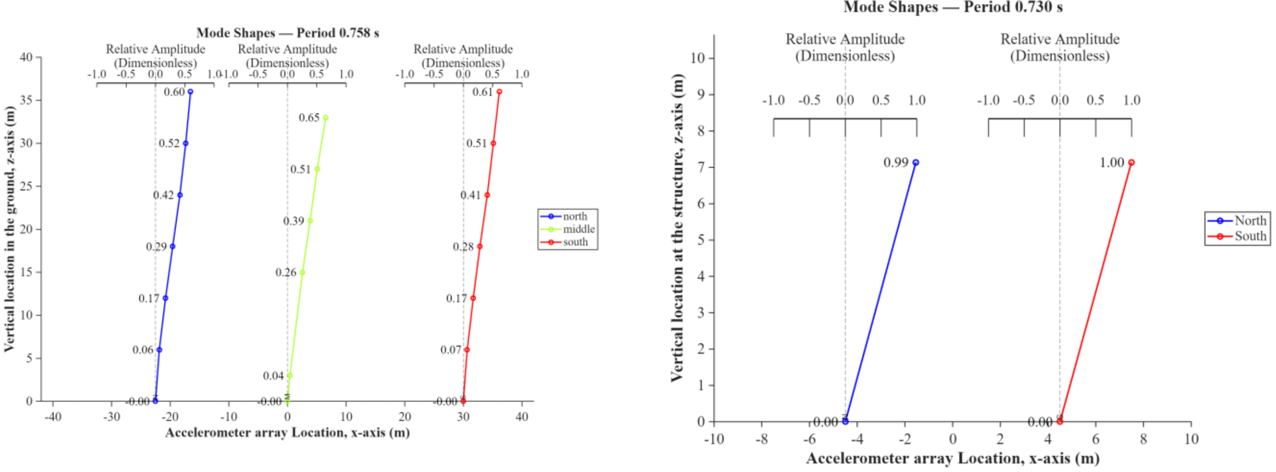

(g) mode shape of ground (h) mode shape of SDOF structure

Fig. A-6 RS, RRS, CPSD and mode shape of ground and SDOF structure Test A1-2, Event 028, Artificial

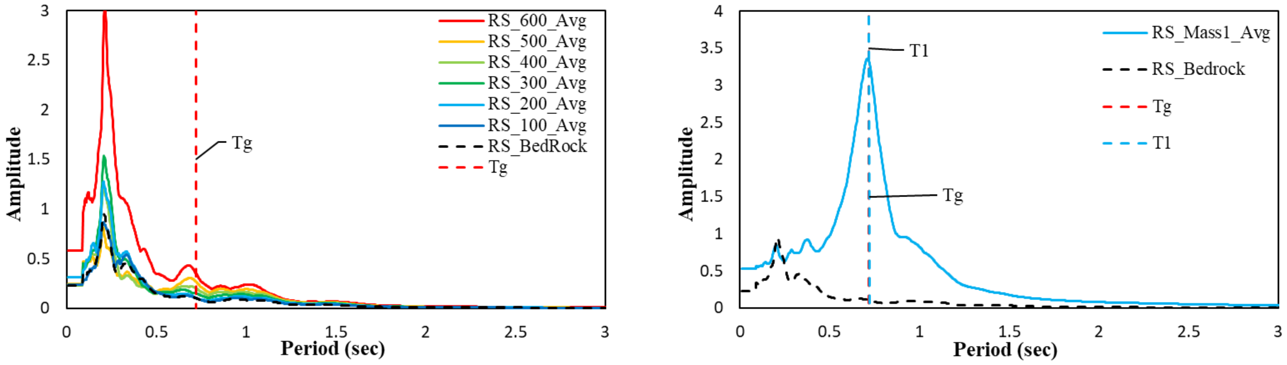

(a) RS of ground (b) RS of SDOF structure

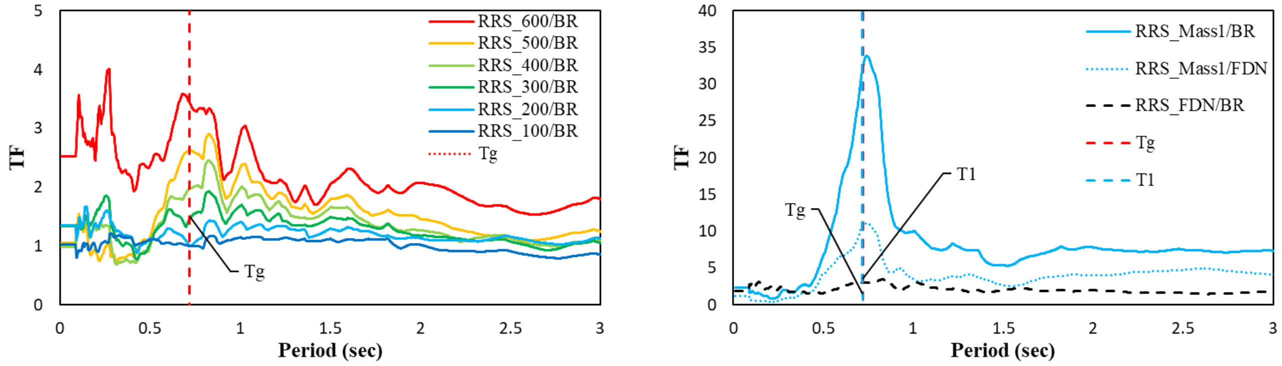

(c) RRS of ground (d) RRS of SDOF structure

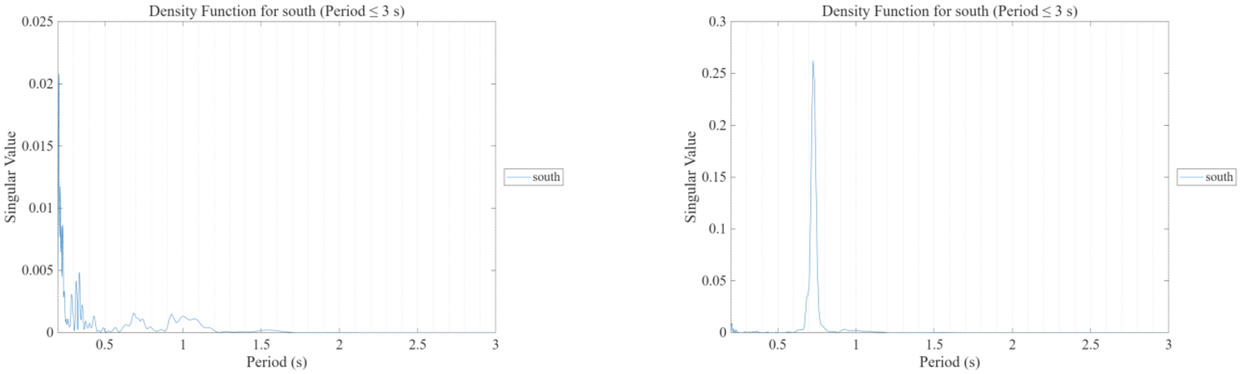

(e) CPSD of ground (f) CPSD of SDOF structure

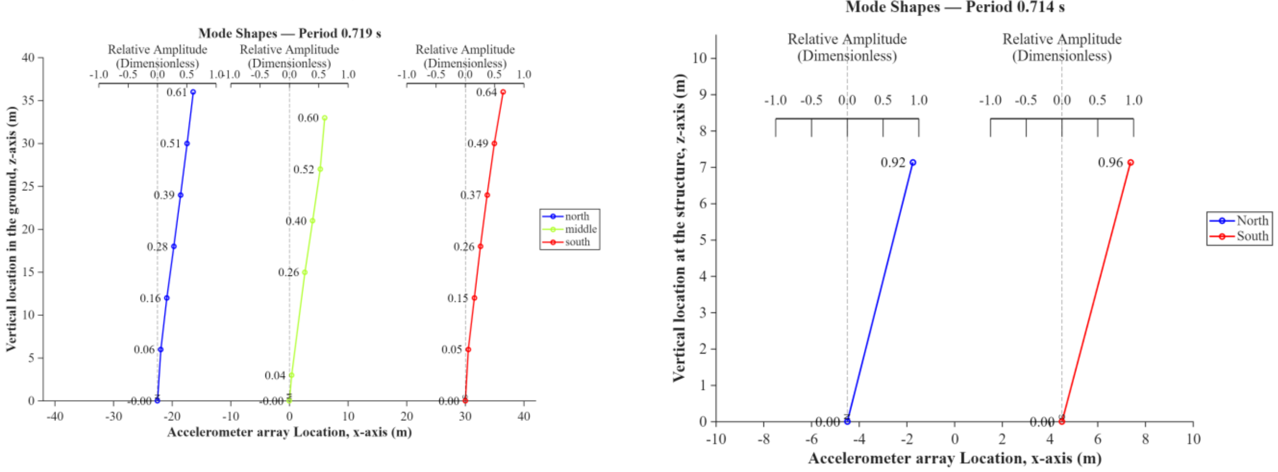

(g) mode shape of ground (h) mode shape of SDOF structure

Fig. A-7 RS, RRS, CPSD and mode shape of ground and SDOF structure Test A1-2, Event 041, Northridge-CIT

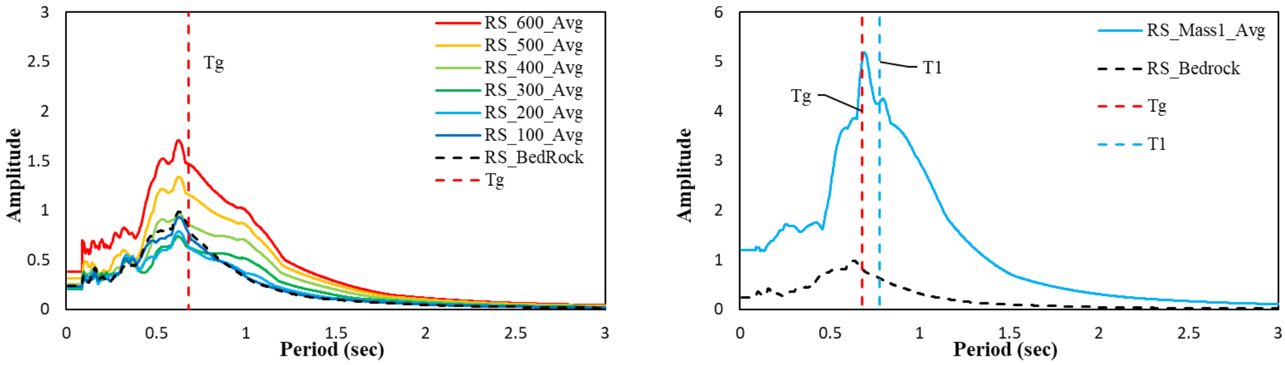

(a) RS of ground

(b) RS of SDOF structure

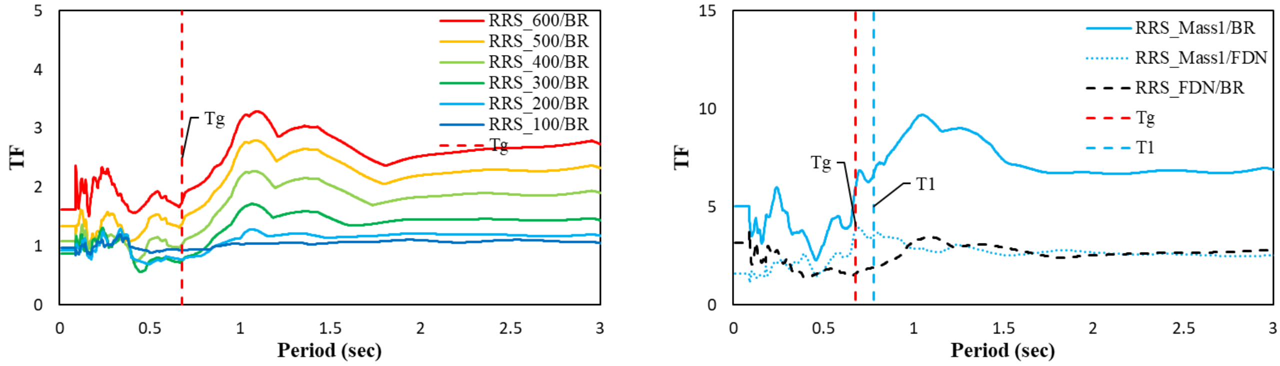

(c) RRS of ground

(d) RRS of SDOF structure

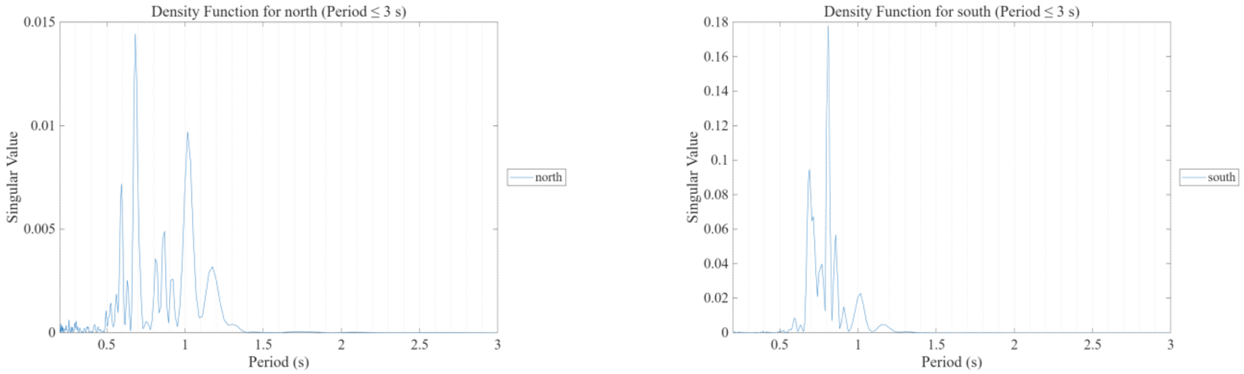

(e) CPSD of ground

(f) CPSD of SDOF structure

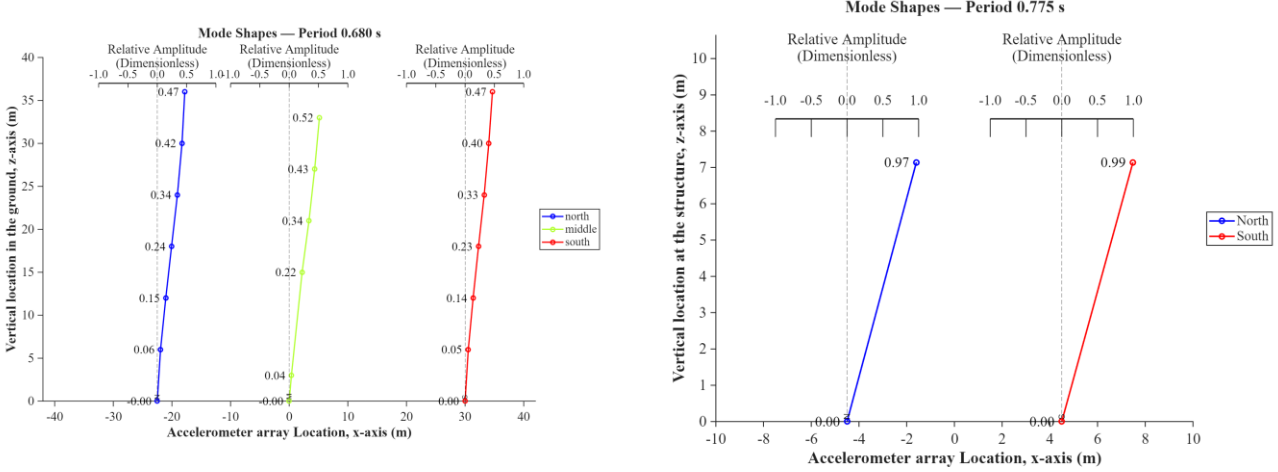

(g) mode shape of ground

(h) mode shape of SDOF structure

Fig. A-8 RS, RRS, CPSD and mode shape of ground and SDOF structure Test A1-2, Event 051, Chuetsu

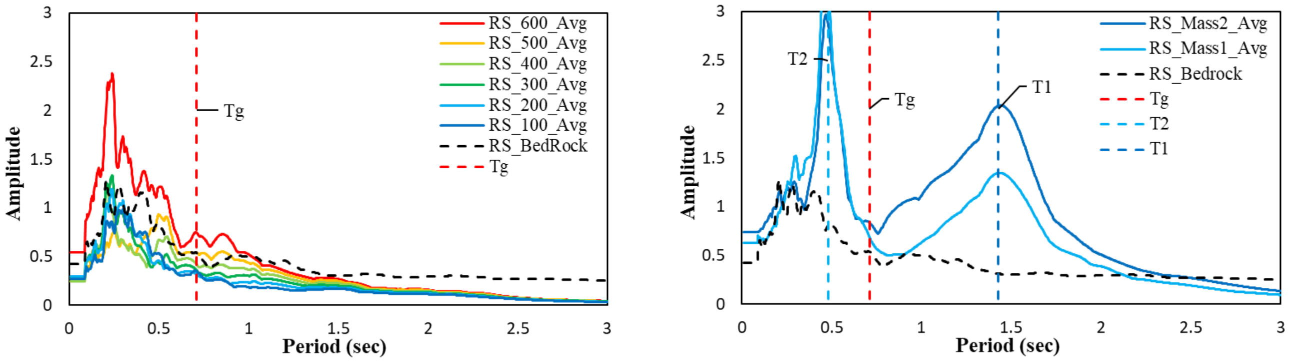

(a) RS of ground (b) RS of 2DOF structure

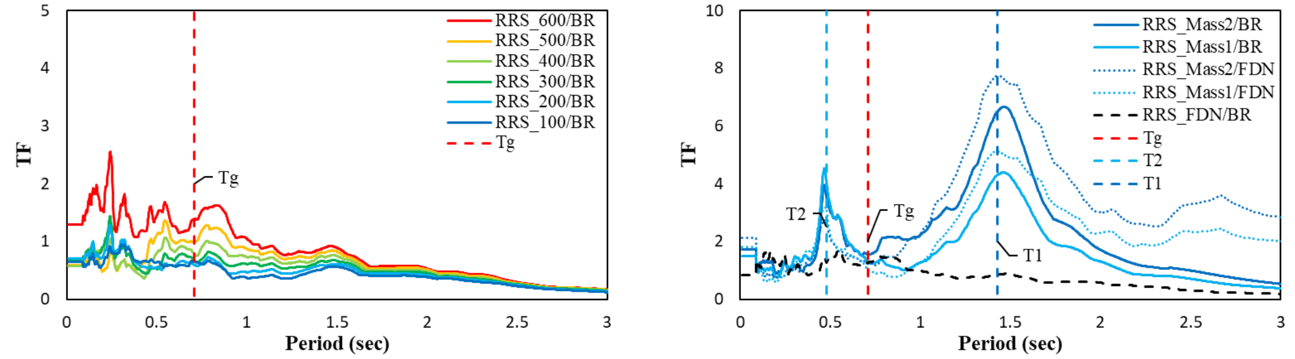

(c) RRS of ground (d) RRS of 2DOF structure

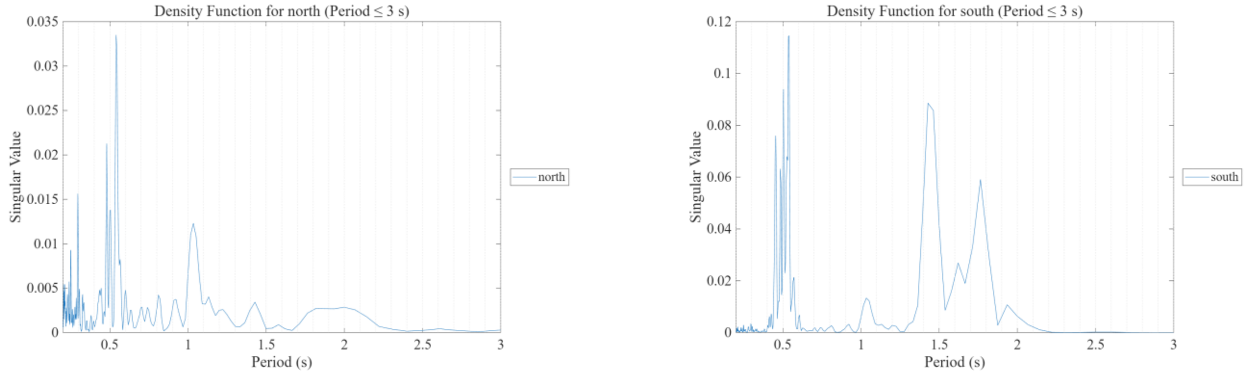

(e) CPSD of ground (f) CPSD of 2DOF structure

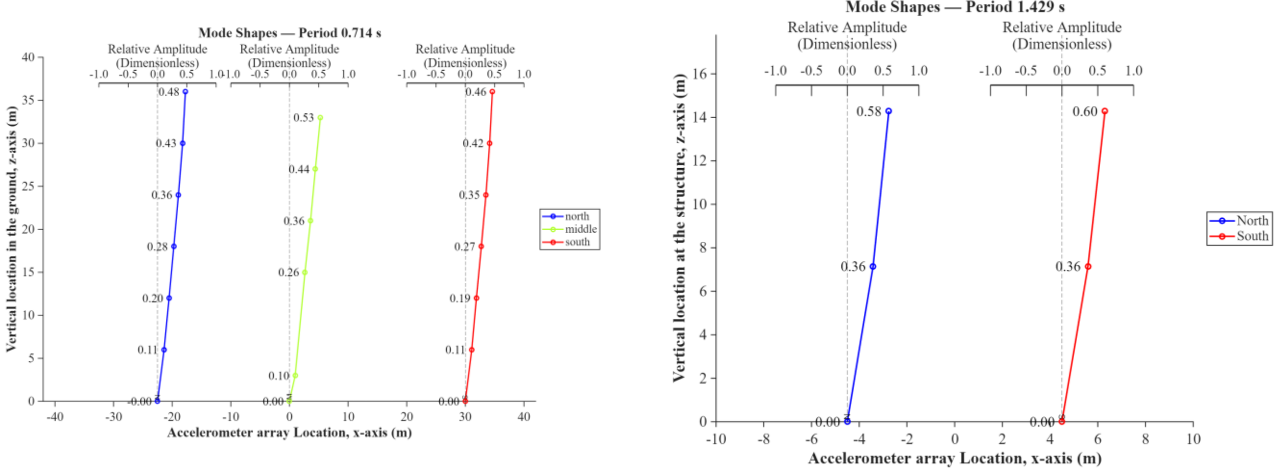

(g) mode shape of ground (h) mode shape of 2DOF structure

Fig. A-9 RS, RRS, CPSD and mode shape of ground and 2DOF structure Test A1-3, Event 020, Kobe-SM

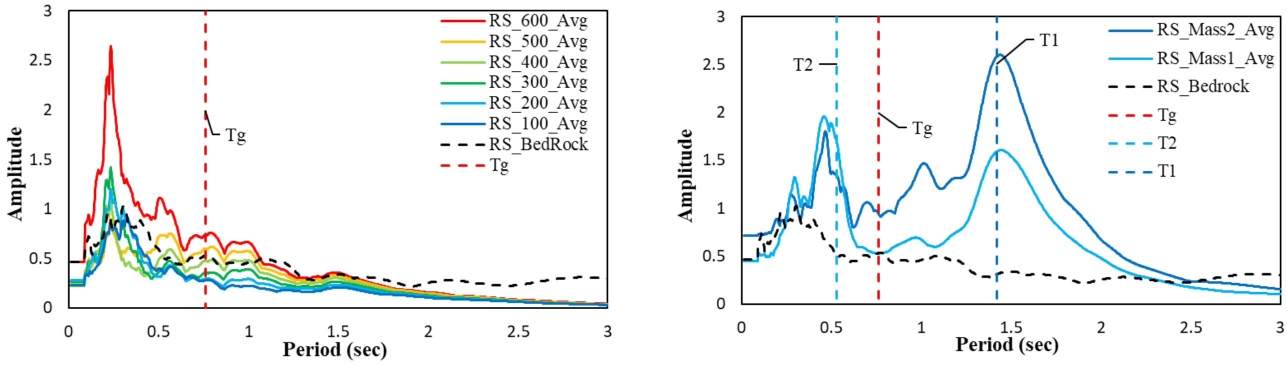

(a) RS of ground (b) RS of 2DOF structure

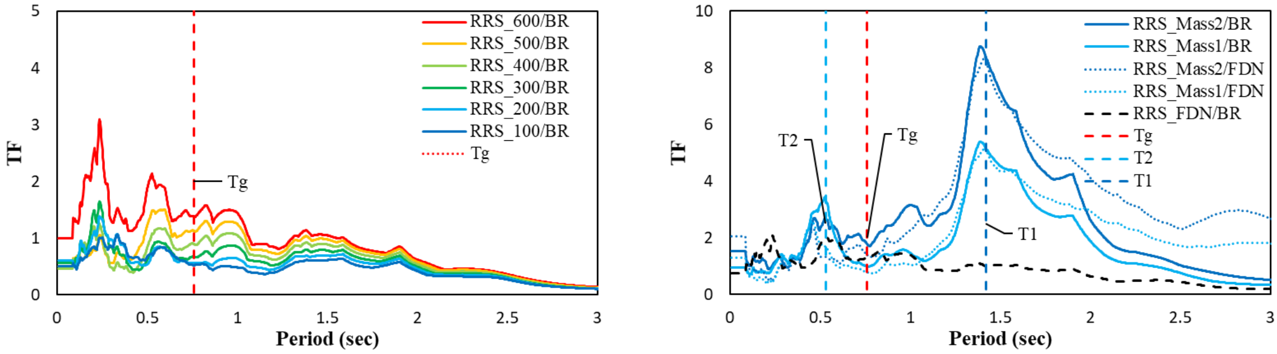

(c) RRS of ground (d) RRS of 2DOF structure

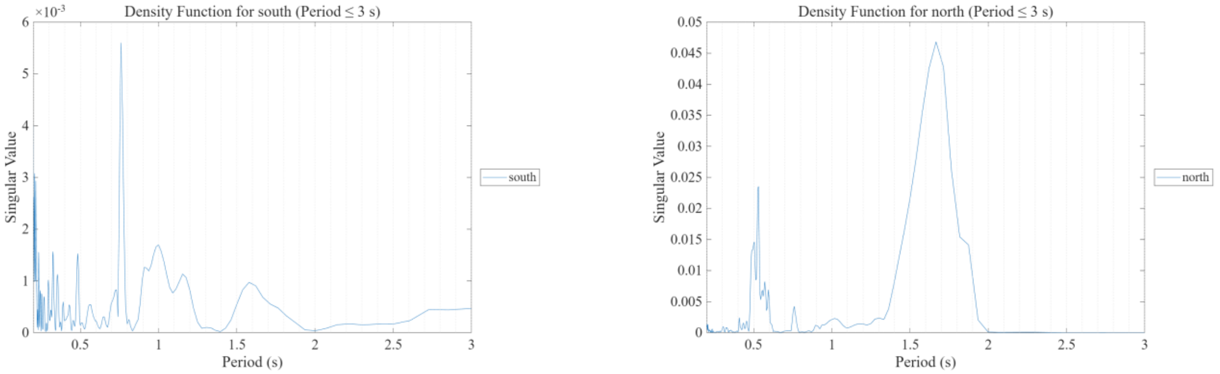

(e) CPSD of ground (f) CPSD of 2DOF structure

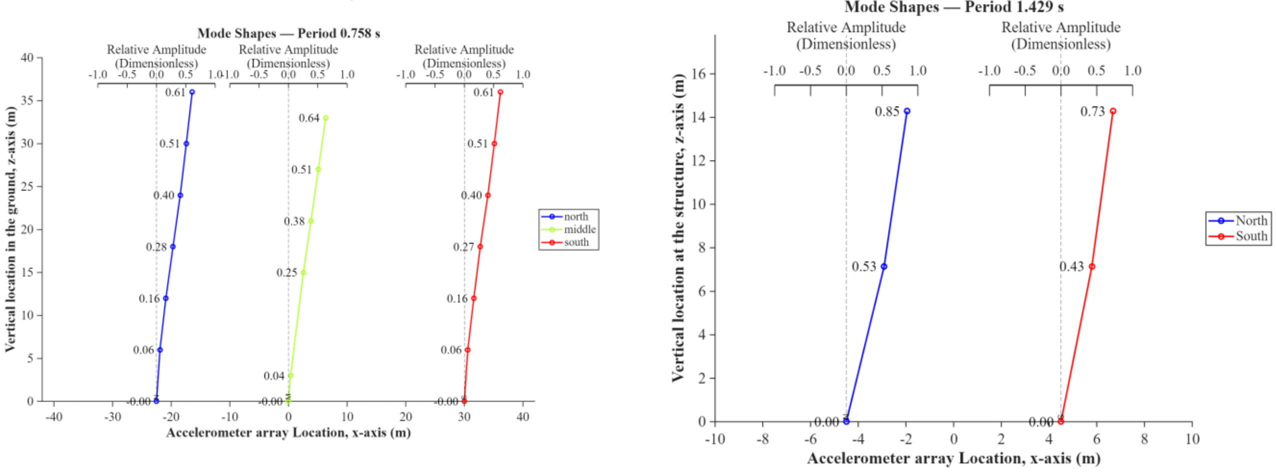

(g) mode shape of ground (h) mode shape of 2DOF structure

Fig. A-10 RS, RRS, CPSD and mode shape of ground and 2DOF structure Test A1-3, Event 028, Artificial

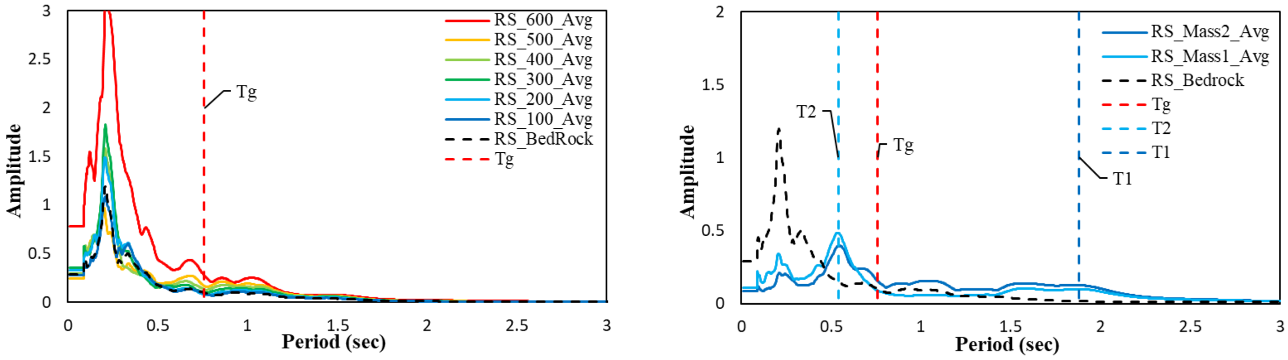

(a) RS of ground (b) RS of 2DOF structure

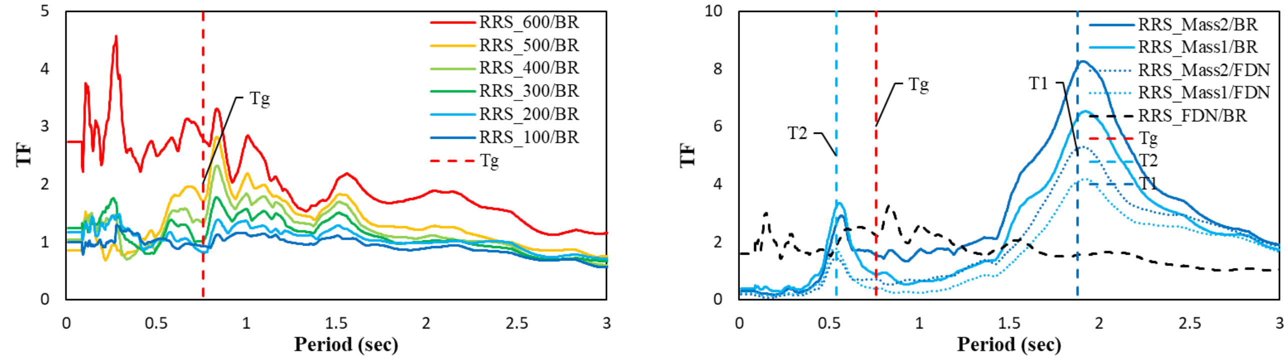

(c) RRS of ground (d) RRS of 2DOF structure

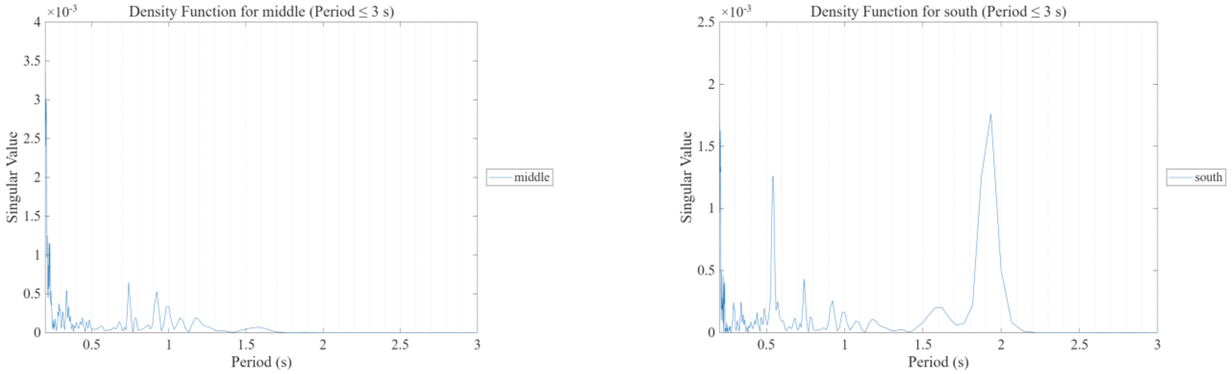

(e) CPSD of ground (f) CPSD of 2DOF structure

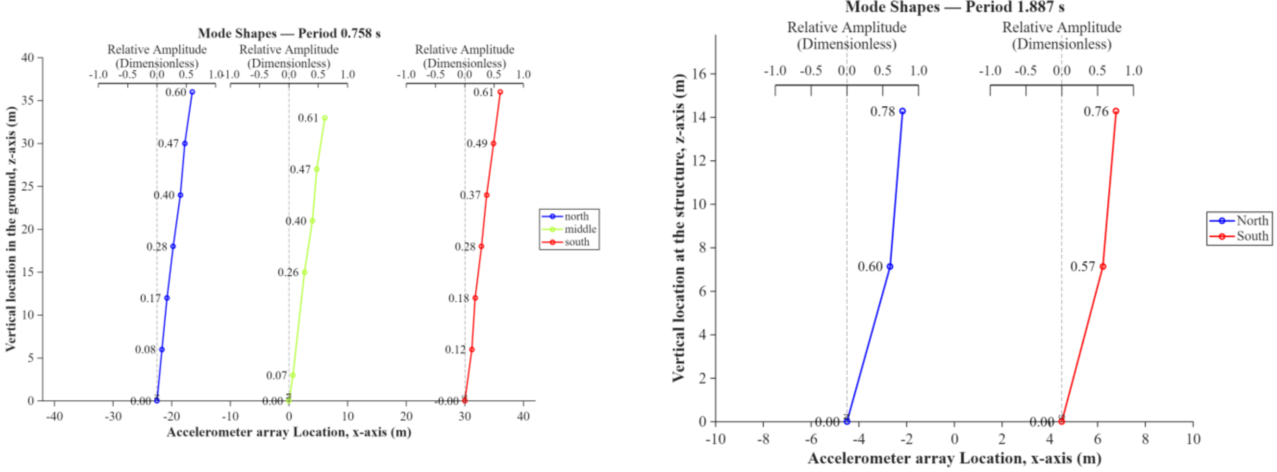

(g) mode shape of ground (h) mode shape of 2DOF structure

Fig. A-11 RS, RRS, CPSD and mode shape of ground and 2DOF structure Test A1-3, Event 036, Northridge-CIT

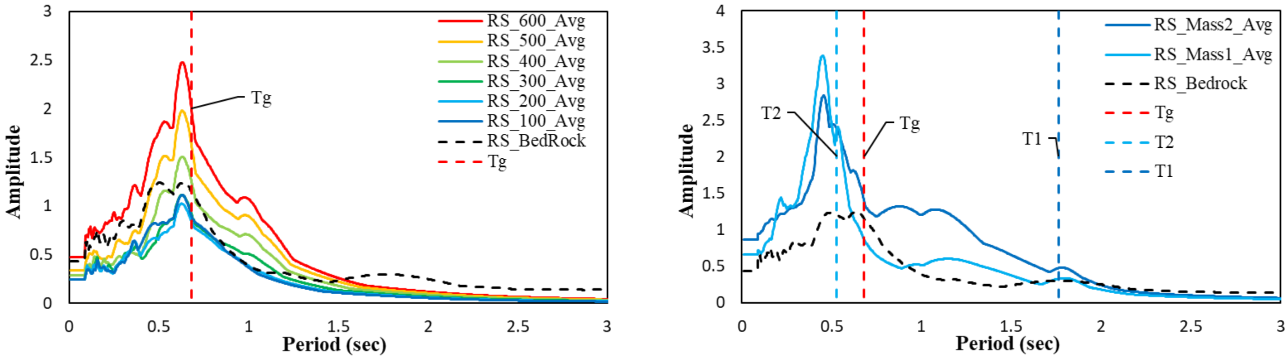

(a) RS of ground (b) RS of 2DOF structure

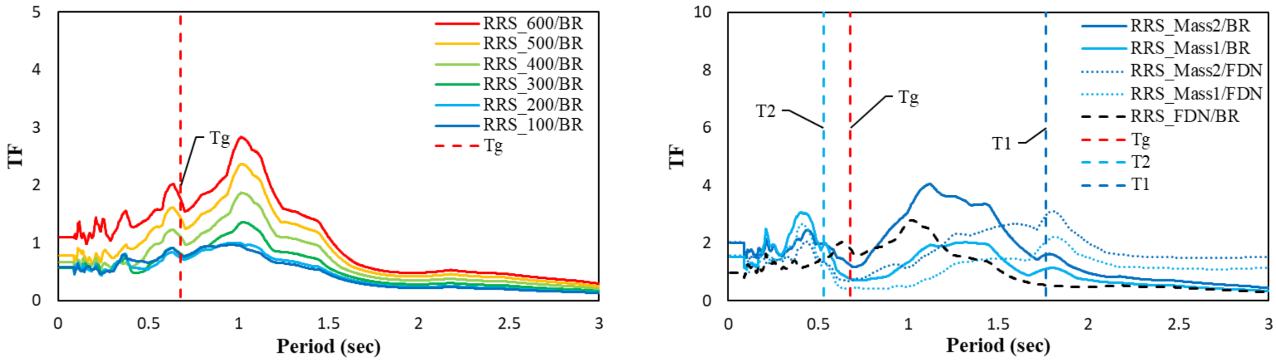

(c) RRS of ground (d) RRS of 2DOF structure

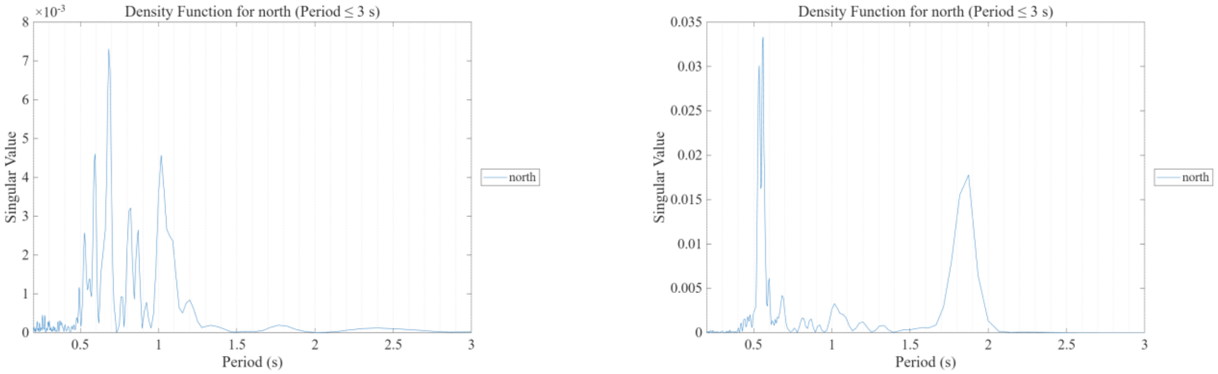

(e) CPSD of ground (f) CPSD of 2DOF structure

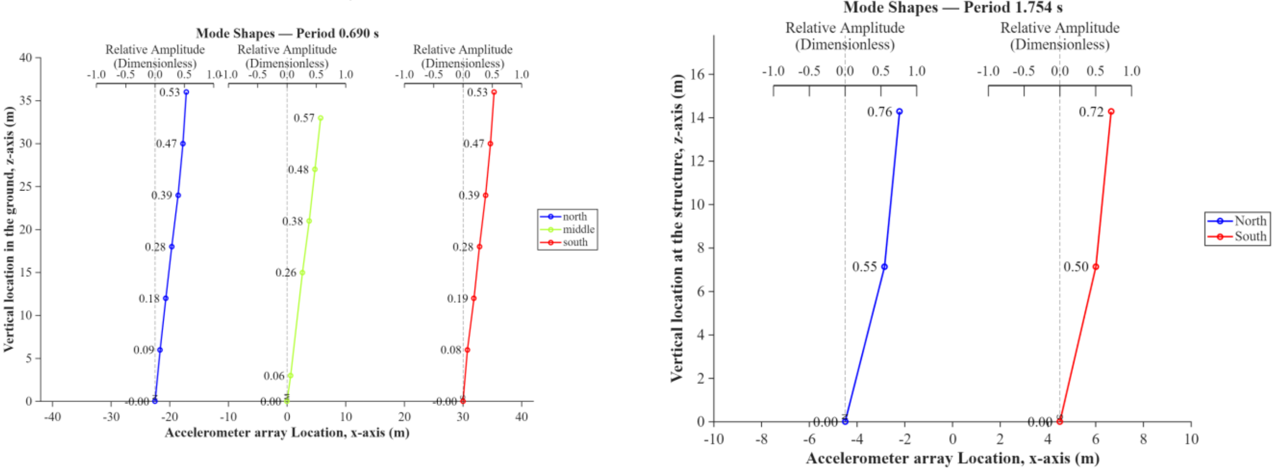

(g) mode shape of ground (h) mode shape of 2DOF structure

Fig. A-12 RS, RRS, CPSD and mode shape of ground and 2DOF structure Test A1-3, Event 040, Chuetsu

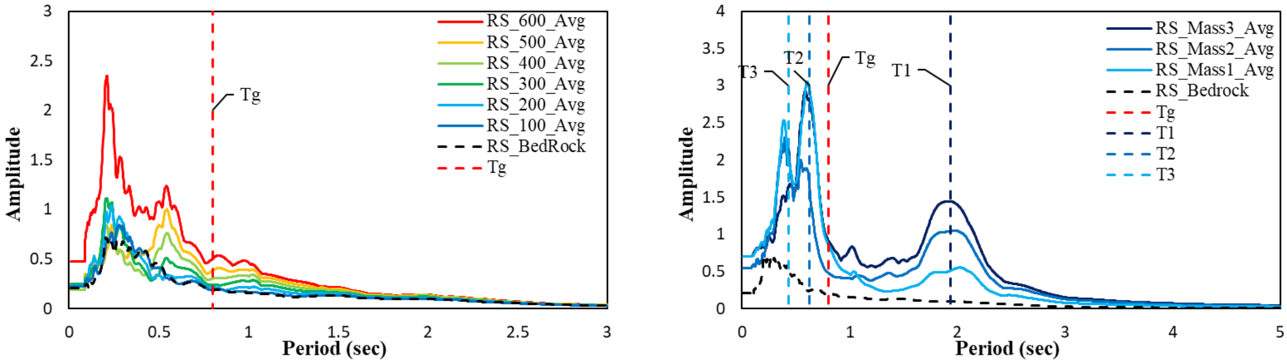

(a) RS of ground (b) RS of 3DOF structure

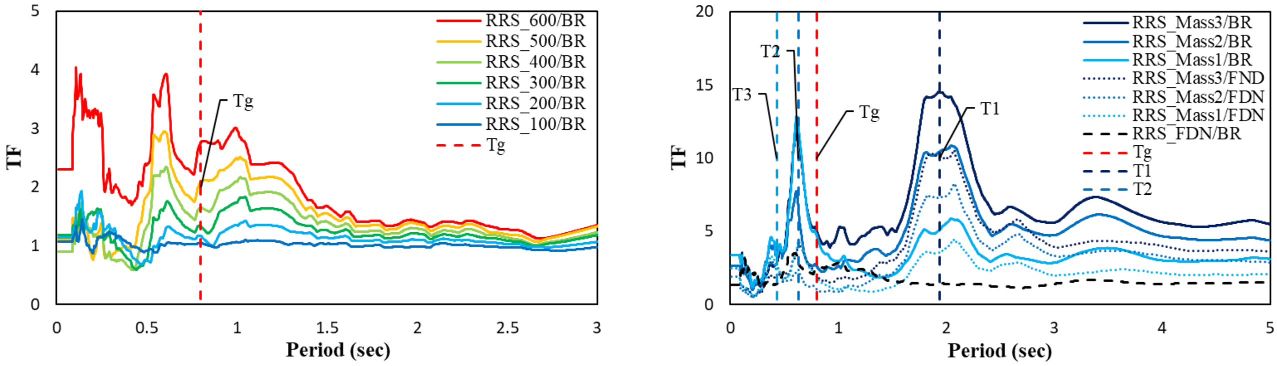

(c) RRS of ground (d) RRS of 3DOF structure

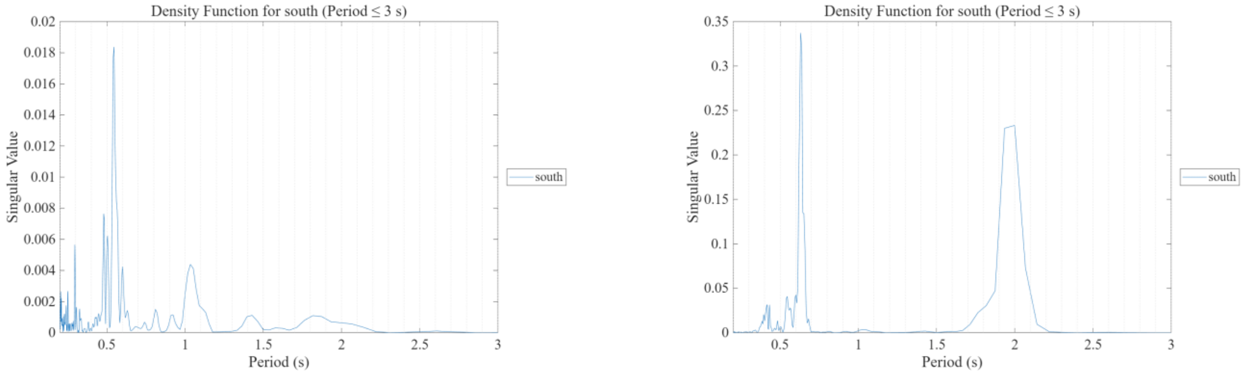

(e) CPSD of ground (f) CPSD of 3DOF structure

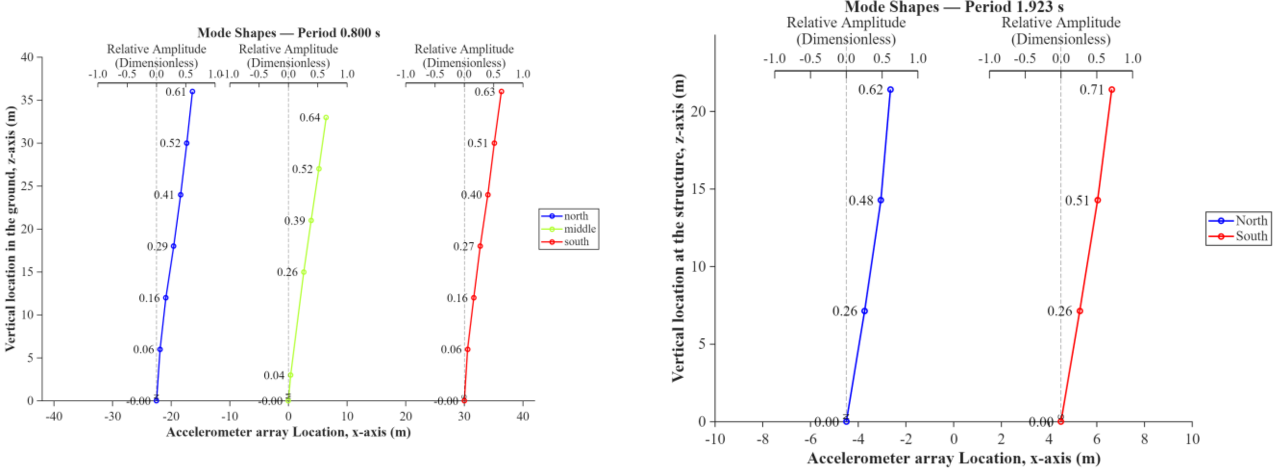

(g) mode shape of ground (h) mode shape of 3DOF structure

Fig. A-13 RS, RRS, CPSD and mode shape of ground and 3DOF structure Test A1-4, Event 017, Kobe-SM

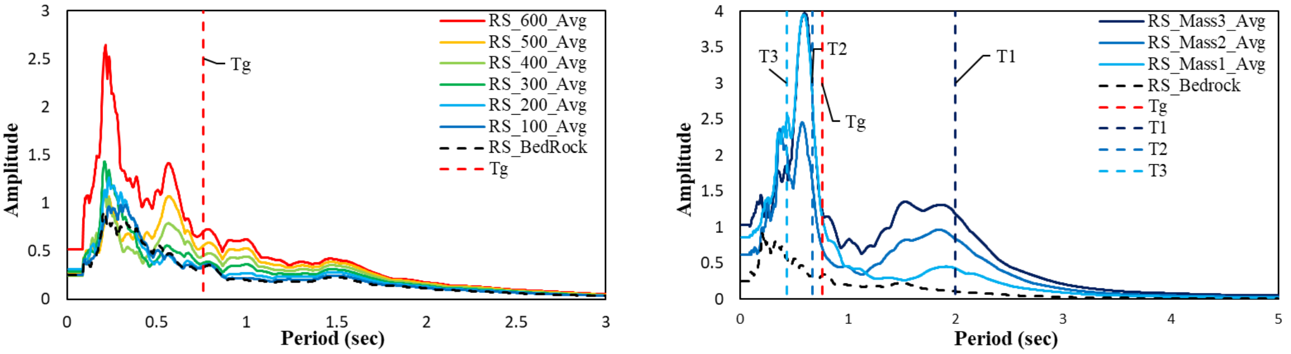

(a) RS of ground (b) RS of 3DOF structure

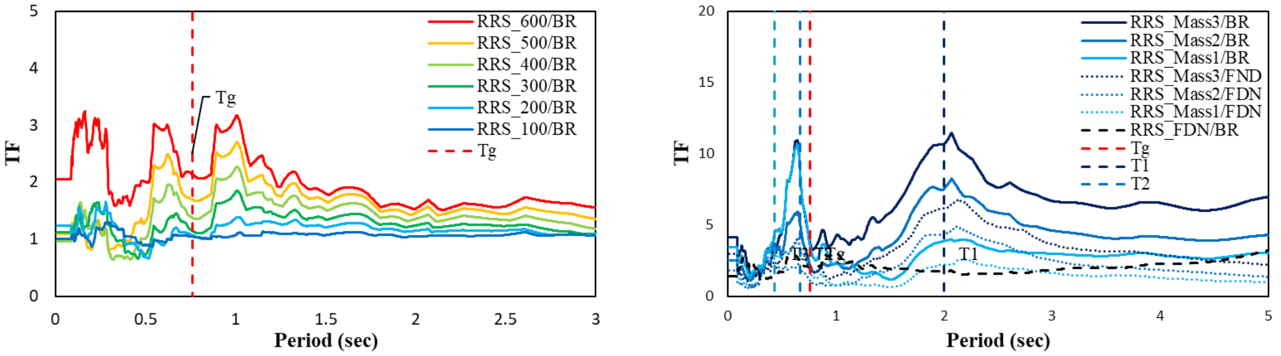

(c) RRS of ground (d) RRS of 3DOF structure

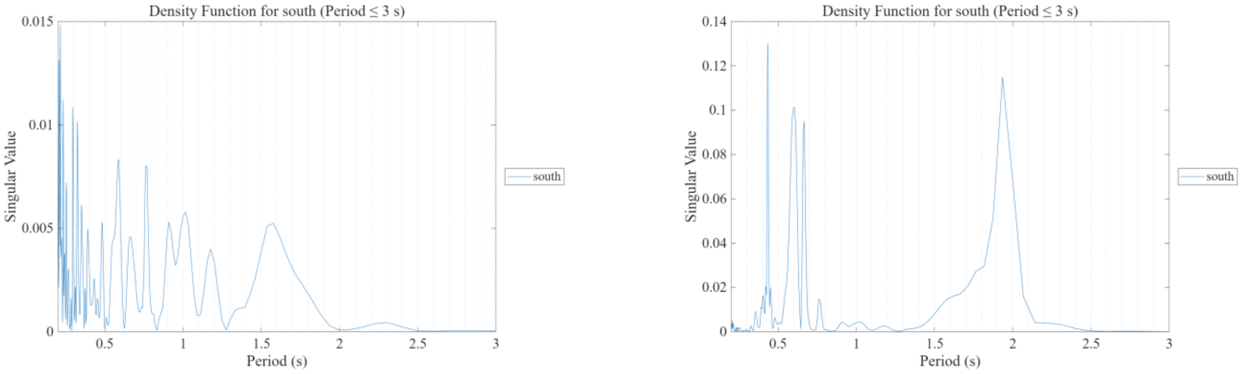

(e) CPSD of ground (f) CPSD of 3DOF structure

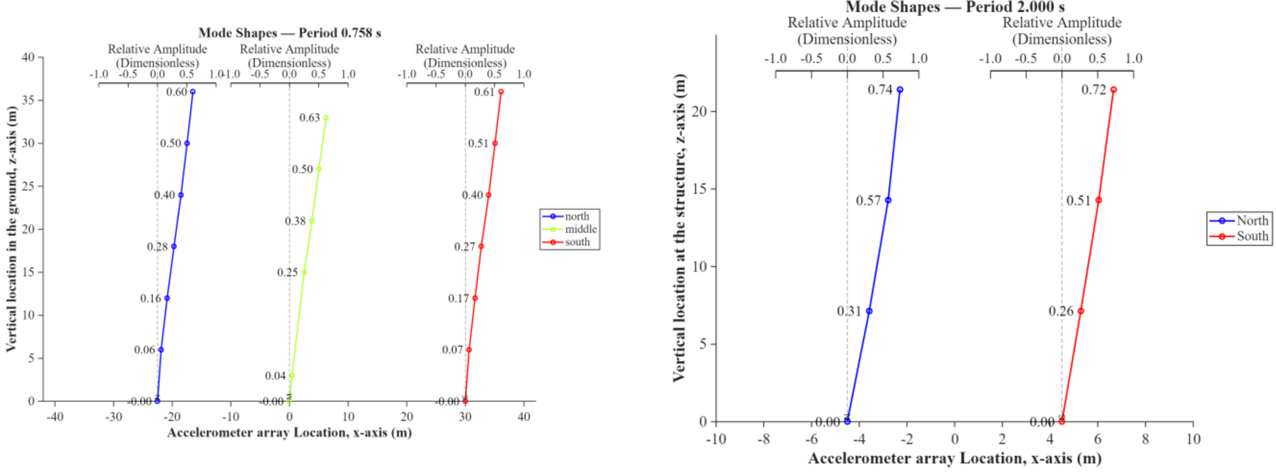

(g) mode shape of ground (h) mode shape of 3DOF structure

Fig. A-14 RS, RRS, CPSD and mode shape of ground and 3DOF structure Test A1-4, Event 024, Artificial

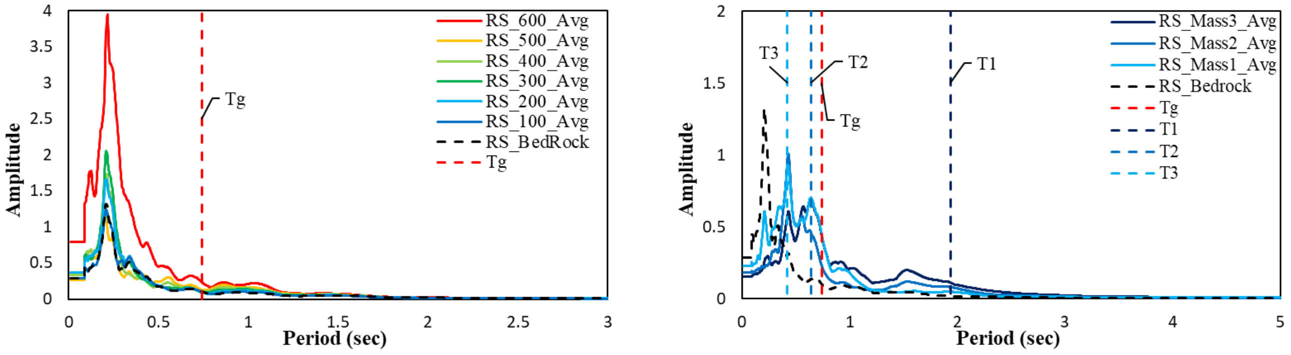

(a) RS of ground (b) RS of 3DOF structure

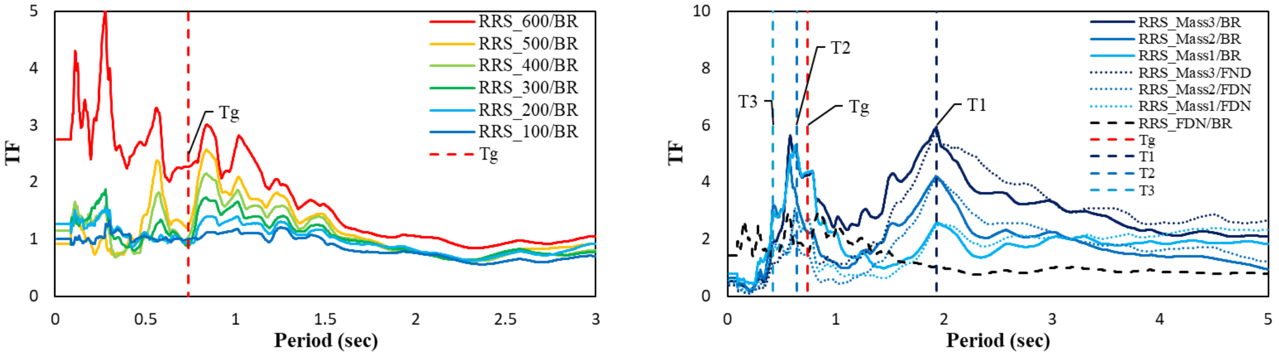

(c) RRS of ground (d) RRS of 3DOF structure

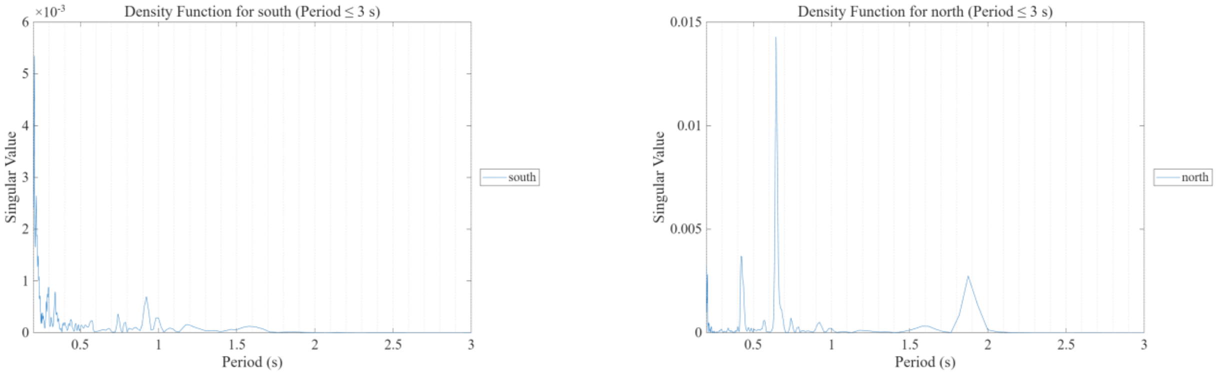

(e) CPSD of ground (f) CPSD of 3DOF structure

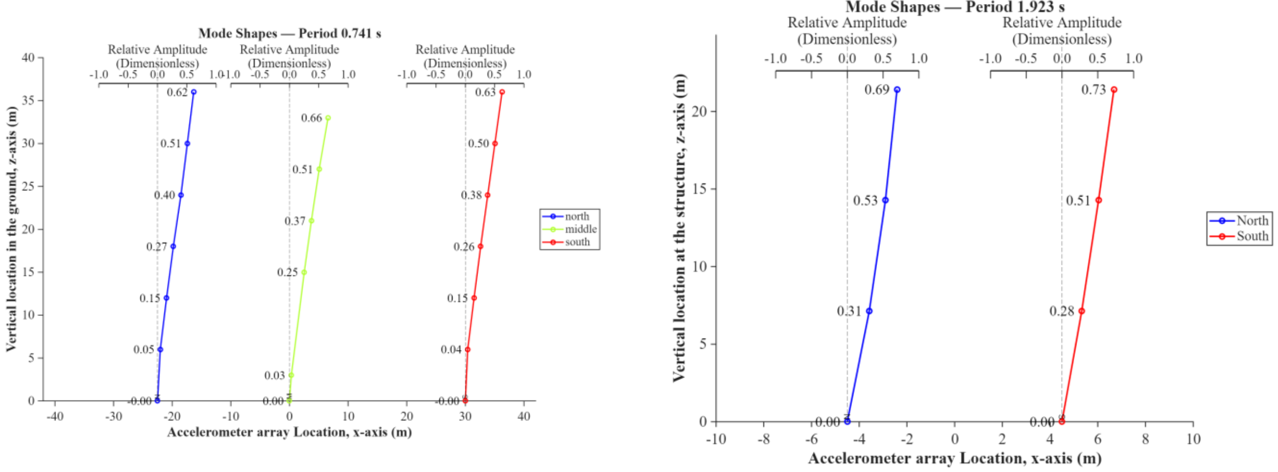

(g) mode shape of ground (h) mode shape of 3DOF structure

Fig. A-15 RS, RRS, CPSD and mode shape of ground and 3DOF structure Test A1-4, Event 032, Northridge-CIT

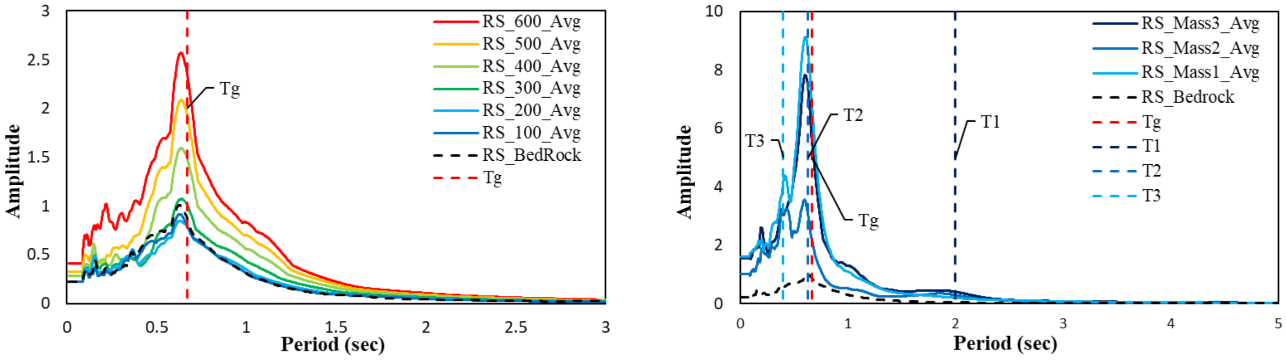

(a) RS of ground (b) RS of 3DOF structure

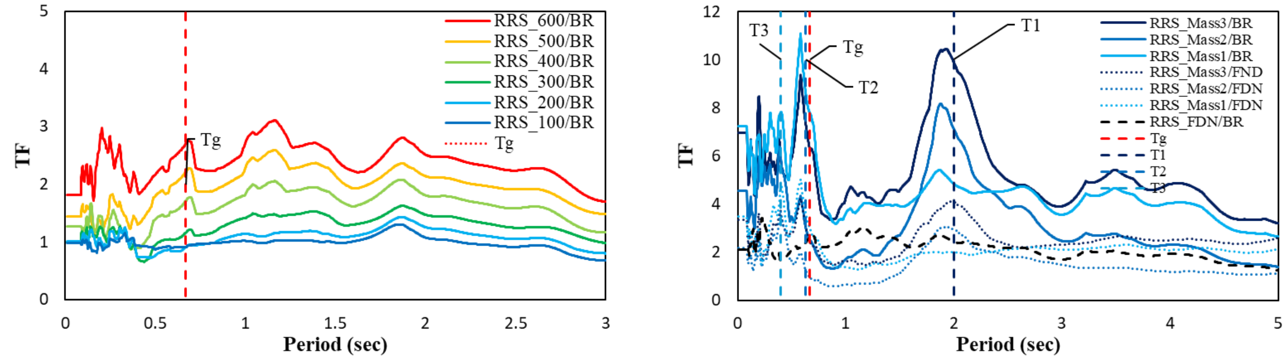

(c) RRS of ground (d) RRS of 3DOF structure

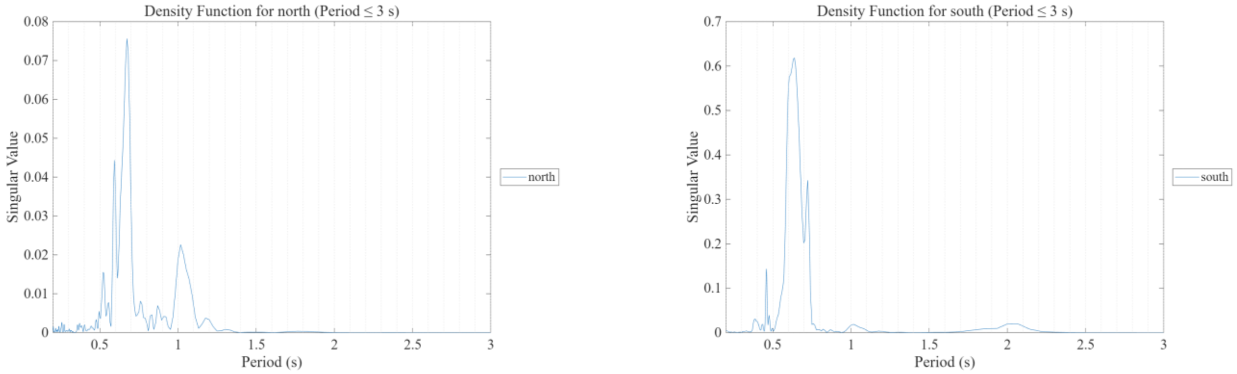

(e) CPSD of ground (f) CPSD of 3DOF structure

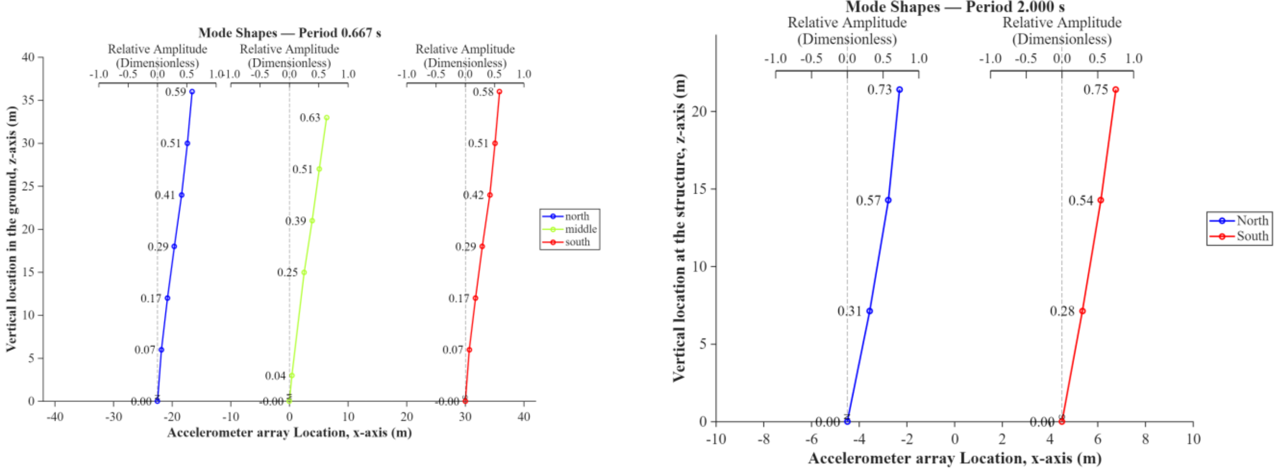

(g) mode shape of ground (h) mode shape of 3DOF structure

Fig. A-16 RS, RRS, CPSD and mode shape of ground and 3DOF structure Test A1-4, Event 041, Chuetsu